Mitigating Optical Crosstalk for In-Situ Mid-Circuit Measurement and Reset in a Trapped-Ion Quantum Simulator

by

Shilpa Mahato

A thesis
presented to the University of Waterloo
in fulfillment of the
thesis requirement for the degree of
Master of Science
in
Physics (Quantum Information)

Waterloo, Ontario, Canada, 2025

© Shilpa Mahato 2025

Author's Declaration

I hereby declare that I am the sole author of this thesis. This is a true copy of the thesis, including any required final revisions, as accepted by my examiners.

I understand that my thesis may be made electronically available to the public.

Abstract

Trapped-ion qubits have emerged as a leading architecture for building both digital and analog quantum computers. Their long coherence times, simple state preparation and measurement procedures, and laser-based qubit manipulation make them a promising platform for quantum information processing. An important feature that can make these systems more fault-tolerant and expand their capabilities to perform different classes of simulation is high-fidelity Mid-circuit Measurement and Reset (MCMR).

Several techniques have been proposed for implementing MCMR in trapped-ion systems. Our group has taken a bold approach by relying on sophisticated optical engineering to generate a low-crosstalk individual addressing beam for performing MCMR. A Digital Micromirror Device (DMD), which is a 2D array of micro mirrors, is used to engineer an incoming wavefront to generate individual addressing beams at the ions using Fourier holography. The technique has been optimized with in-situ aberration compensation and the use of Iterative Fourier Transform Algorithm (IFTA) for hologram generation, forming the current state-of-the-art individual addressing system.

In this thesis, two methods have been proposed that further strengthen our addressing system, making it more robust against measurement errors introduced by intensity crosstalk. The proposed methods, secondary grating method, and using the DMD in a double pass configuration have been successful in minimizing the absolute intensity crosstalk at the nearest neighbor and at the asymptotic limit. These improvements will have a significant impact on the current standing of MCMR fidelities in trapped-ion qubits.

Acknowledgements

Fresh out of my bachelor's, I knew I wanted to pursue two things: optics and experimental quantum information. I am deeply grateful to Dr. Kazi Rajibul Islam for giving me the opportunity to explore both at the Quantum Information with Trapped Ions (QITI) lab. I appreciate his guidance, thoughtful feedback, and constant encouragement, which pushed me to improve my scientific aptitude and positively influenced my overall outlook in life.

I would like to thank my advisory committee members, Dr. Michel Gingras and Dr. Dmitry Pushin, for their valuable feedback during the committee meetings, which helped me improve both my research and presentation.

I want to thank my wonderful colleagues at the QITI lab who made working ten times more fun and engaging. I want to thank the former members of the group, Gilbert, Sainath, and Nikhil, for sharing their expertise with me. Thanks to the Amethyst team, Yu-Ting, Anthony, Monica, and Siddharth, for being proactive in answering all my questions. I want to thank the Bloodstone team, Lewis, Fabien, and Sakshee, for being my rock, and the Quantum-ION team, Akbar, Ali, Aki, and Hawking, for open discussions about science. I appreciate all the work put in by the co-ops to make our experiments successful. Special shout-out to Monica and Sakshee for keeping my feminine energy activated.

I want to thank all my friends in Waterloo who made my life easier, and especially my roommates at 185 Pinegrove for making me delicious dinners.

I am grateful to my friends from my undergraduate years who pushed me to do science. Thanks to Aryan for giving me a healthy competition, and Dhyey, Priyanshi, Pranitha, Surya, and the endless list of people who have been there for me.

Thanks to my grandparents for being an inspiration as educators and philanthropists. Lastly, thanks to my parents and my brother for setting an example and supporting my life choices.

Dedication

This is dedicated to those who pursue truth in science, and those who survive the truths the world often refuses to see.

Table of Contents

Author's Declaration ii

Abstract iii

Acknowledgements iv

Dedication v

List of Figures ix

List of Tables xv

List of Abbreviations xvi

1 Introduction 1

1.1 Trapped-Ion Quantum Simulator 2

1.1.1 Bloodstone Processor 4

1.2 Thesis Overview 6

2 Engineering a low-crosstalk individual addressing beam 7

2.1 Overview 7

2.1.1 Chapter Outline 9

2.2 State Detection and Reset in $^{171}Yb^{+}$ 9

2.2.1 State Detection . . . 10
2.2.2 State Reset . . . 11
2.3 Sources of error . . . 12
2.3.1 Finite intensity crosstalk . . . 13
2.3.2 Inter-ion scattering . . . 15
2.4 Existing techniques . . . 16
2.4.1 Scope of Improvement . . . 17
2.5 Fourier Holography with a DMD . . . 19
2.5.1 Working principle . . . 19
2.5.2 Reprogrammable Hologram with DMD . . . 20
2.5.3 Amplitude grating and IFTA . . . 21
2.6 Aberration Compensation . . . 25
2.6.1 Summary and Outlook . . . 27

3 A Secondary Grating Method **28**
3.1 Overview . . . 28
3.1.1 Chapter Outline . . . 29
3.2 Theoretical Background . . . 30
3.3 Experimental Setup . . . 32
3.3.1 Bloodstone Parameters . . . 33
3.3.2 Optical Schematic . . . 35
3.3.3 Methodology . . . 36
3.4 Results: Measurement of Intensity Crosstalk . . . 37
3.4.1 Focal length calibration . . . 37
3.4.2 Camera calibration . . . 37
3.4.3 Aberration Data . . . 37
3.4.4 Intensity Crosstalk Data . . . 38
3.4.5 2D scan . . . 41
3.4.6 Error Analysis . . . 44
3.5 Summary and Discussion . . . 47

4 DMD as a Double Pass **48**

4.1 Overview . . . 48

4.1.1 Chapter Outline . . . 49

4.2 Theoretical Background . . . 50

4.3 Experimental set-up . . . 51

4.3.1 Optical Schematic . . . 51

4.3.2 Engineering Challenges . . . 53

4.3.3 Methodology . . . 55

4.4 Results: Measurement of Intensity Crosstalk . . . 57

4.4.1 Aberration Data . . . 57

4.4.2 Beam Location Calibration . . . 58

4.4.3 Intensity Crosstalk Data . . . 59

4.4.4 Error Analysis . . . 63

4.5 Summary and Conclusion . . . 64

5 Conclusion and Outlook **65**

References **67**

List of Figures

1.1 Figure shows the energy level diagram for $^{171}Yb^{+}$ 3

1.2 Figure showing a four-rod Paul trap 4

1.3 Qubit states, $|\uparrow\rangle$ and $|\downarrow\rangle$ represented by $^{2}S_{1/2}\,|F=1, m_F=0\rangle$ state and $^{2}S_{1/2}\,|F=0, m_F=0\rangle$ state, respectively. The qubit frequency is given by $2\pi \times 12.6$ GHz. 4

1.4 Top left shows the vacuum chamber, which houses the ion trap. Top right shows the cross-section of the blades as seen from the front of the chamber. Bottom left shows a CAD model of the segmented blades, which serve as the electrodes. Bottom right shows a single blade where the marked central segment serves as the main trapping region. 5

1.5 Fluorescence observed from a chain of 25 $^{171}Yb^{+}$ ions trapped in the Bloodstone processor when illuminated with a 369 nm laser beam corresponding to the transition $^{2}S_{1/2} \rightarrow {}^{2}P_{1/2}$ 6

2.1 Schematic representation of state detection procedure in $^{171}Yb^{+}$. 10

2.2 Schematic representation of state reset procedure in $^{171}Yb^{+}$. 12

2.3 Demonstration of AQM 13

2.4 Figure demonstrating an imperfect addressing beam with some finite intensity crosstalk at ion 1 or the asset qubit. I_X defines the relative intensity crosstalk between ion 2 and ion 1. The magnetic field direction is perpendicular to the ion-chain as well as the direction of the addressing beam. . . 14

2.5 Figure demonstrating inter-ion scattering (red) under the conditions of a perfect addressing beam with no intensity crosstalk, I_X at ion 1. 15

2.6 Figure showing the dependence of wave vector ($k_{i=0,1}$) at the FP with spatial position in IP ($x_{i=0,1}$). The electric field at the FP can be represented as a sum of infinite plane waves (k_i), each of which corresponds to different spatial locations (x_i) at the IP. 19

2.7 Flowchart for IFTA 24

2.8 Left shows a virtual image of the DMD in the FP, where two patches (not to scale) have been turned on. Right shows an image of the interference pattern as seen on a camera. The axes on the camera (IP) are tilted by a 45° angle since the DMD is mounted at 45° on the optics table to ensure the propagation direction of the reflected beam is parallel to the optics table (Figure 3.3). 26

3.1 Left shows a picture of the grating state of the DMD. There is a larger grating in the background which corresponds to the primary grating. Lying on top of the primary grating is a secondary grating within a rectangular window ($l \times m$). Right shows a picture of Image Plane 1 (IP1) where the primary beam falls on the mapped position of Ion 2 (process qubit) in the IP1. The secondary beam falls on the mapped position of Ion 1 (asset qubit). The ion-to-ion separation is given by a. We can optimize the phase and amplitude of the secondary beam by changing the phase (ϕ_2) and the amplitude (A_2') parameters in the secondary grating to create a local destructive interference. 31

3.2 ON and OFF state of the DMD micro mirrors with respect to the flat reference position 33

3.3 DMD (DLP9000XUV) mounted at a 45° angle. 34

3.4 A qualitative schematic of the whole relay optics for the individual addressing beam. The DMD is shown as a transmissive element for simplicity. . . 35

3.5 Optical schematic for the secondary grating method. 36

3.6 Plot between periodicity of grating corresponding to different beam positions along ion chain axis and the beam position extracted from the camera. The curve is fitted to a linear model and the effective focal length obtained is 161 mm. 38

3.7 Figure showing calibration of the camera (FLIR BFS-PGE-120S4M-CS) used for data extraction. A linear change in the pixel value can be seen with the increase in input power of the beam falling on the camera. 39

3.8 Aberration phase map (Radius of the Fourier plane is 700 pixels) (a) $\Phi_0(x)$ is measured to be 9.8λ (19.6π) peak-to-peak and 1.75λ RMS. (b) $\Phi_1(x)$ is measured to be 2.01λ (4π) peak-to-peak and 0.4λ RMS. 40

3.9 **Linear Scale Data**: Pixel value at $x = 4w_{\text{IP1}}$ from the primary beam alone is 79. (a) Phase (ϕ_2) of the secondary beam is scanned keeping the amplitude (A_2') fixed at 0.7 and the pixel value at $x = 4w_{\text{IP1}}$ is plotted. Suppression of I_X can be seen for $\phi_2 = \pi$ where the pixel value dips to 50, i.e. 36% suppression. (b) Amplitude (A_2') of the secondary beam is scanned keeping the phase (ϕ_2) fixed at π and the corresponding pixel value at $x = 4w_{\text{IP1}}$ is plotted. A further suppression in the pixel value to 43, i.e. 38.6% can be seen for $A_2' = 0.44$. The error bars represent the standard error for 3 shots, where each shot represents an image taken on the camera for an exposure value of 1.2 s. 42

3.10 **HDR Data**: I_X from primary beam is $10^{-4.3}$. (a) Phase (ϕ_2) of the secondary beam is scanned keeping the amplitude (A_2') fixed at 0.7, and the normalized I_X obtained from the HDR images is plotted. Suppression in I_X by ≈ 5 dB can be seen for $\phi_2 = \pi$. (b) Amplitude (A_2') of the secondary beam is scanned keeping the phase (ϕ_2) fixed at π and the corresponding normalized I_X is plotted. A further suppression of I_X, i.e., ≈ 6 dB, is seen after optimizing A_2' to 0.38. The error bars represent the standard error computed from 3 HDR images computed from taking 3 shots of images at exposure settings ranging from 120 μs to 12 s. 43

3.11 A 2D colourmap representing the I_X for different values of phase ($\phi_2 \in [0, 4\pi]$) and amplitude ($A_2' \in [0, 1]$). Periodic pockets of minima can be seen in amplitude and phase space as expected from Equation 3.9. Primary grating crosstalk (marked in red) refers to the I_x (Pixel value at $4w_{IP1}$) when only the primary grating is displayed on the DMD. 44

3.12 A standard error map for the for the 2D scan mentioned in Figure 3.11 with mean standard error of 0.82. 45

3.13 Plot showing different beam locations as seen on the camera at IP1 for different data points in the 2D scan shown in Figure 3.11. The color map shows the frequency of occurrence for a particular beam center location. . . 46

3.14 Figure showing the actual intensity profile of the primary beam, with the moving average/smoothened curve with 10 pixels. The shaded pink region shows the estimated maximum and minimum fluctuations in the intensity. 46

4.1 A simplified schematic presenting the idea of using a pupil to act as a filter at the intermediate image plane (IP1). This pupil is used to essentially block the asymptotic tail of the Gaussian distribution of the intensity of the addressing beam, thus reducing I_X outside the region of the pupil. DMD has been shown as a transmissive element for simplicity. 50

4.2 Optical Schematic for the DMD as a Double Pass method. The DP retro-reflector board is placed on a stage to control the location of IP1. AS1 and AS2 refer to Aperture Stop 1 and 2, respectively. The size of the DMD is not to scale for more clarity. 52

4.3 (a) Demarcation between the FP1 [0, 2060] (the 100 pixels buffer is included here) region and IP1 [2060, 2560] region of the DMD is shown. (b) A 3D printed iris for optical separation of the input beam to FP1 from IP1. The size of the iris is chosen to match the dimensions of FP1. 53

4.4 (a) Image of the first and zeroth order Gaussian beam reflected from the IP1 (DMD) for a particular amplitude grating hologram. (b) Image of the first and zeroth orders for two patches turned on at the center reference and at some other point in the grid. The multiple diffraction orders seen in (a) and (c) are a result of diffraction effects from the natural grating of the micro mirrors in the DMD. (c) DP (Double Pass) retro-reflector board: A board machined to serve as a retro-reflector with the Fourier lens sandwiched in between two bending mirrors. 54

4.5 (a, b) An iris is used at the FP2 to filter out the beam from the undesired orders. The size of the iris has to be adjusted such that the light reflected from the scanning patch of the desired order can make it through the iris while blocking the other beams corresponding to the undesired orders. . . . 55

4.6 This picture gives a relative idea about the direction of the incoming beam, reflection from the protective glass window on the DMD and the reflection from the micro mirror array. 56

4.7 (a, b, c) Aberration maps corresponding to $\Phi_0(x)$, $\Phi_1(x)$ and $\Phi_2(x)$ respectively. (d) This is the residual aberration map obtained after compensating for the aberrations using $\Phi_0(x) + \Phi_1(x) + \Phi_2(x)$. (Radius of the Fourier plane is 700 pixels) 57

4.8 Figure showing Zernike decomposition of (a) $\Phi_2(x)$ and (b) the residual phase map obtained after aberration compensation. This is obtained by mapping the phase maps to Zernike polynomials, which are a sequence of polynomials orthogonal in nature and defined on a unit circle. The x-axis denotes the Zernike polynomials (Z_n^m) corresponding to different aberration types, while the y-axis shows their coefficients, indicating the strength of each aberration. The dominant aberrations are astigmatism [(2,-2),(2,2)] and defocus [(2,0)] for both (a) and (b). 58

4.9 (a) Figure showing the voltage signal (10 shots) as seen on an oscilloscope connected to the output of the photodiode at the IP2, as micro mirrors are turned on, one at a time in a selected 20×20 grid at the IP1 (DMD). The gain of the photodiode is set to maximum to obtain best signal-to-noise ratio. Here, the maximum voltage corresponds to 1.5 V with a background noise of 0.09 V. (b) The standard deviation map for different shots is plotted with a maximum standard error of 0.07 V. 59

4.10 (a) HDR image of a Gaussian beam when DMD is used as a single pass. (b) HDR image of a Gaussian beam when the DMD is used as double pass and all the mirrors are turned on at the IP1 (infinite pupil). There is an increase in noise compared to (a) due to scattering from the configuration of the micro mirrors in the DMD, which do not form a single continuous plane (c) HDR image of a Gaussian beam when the DMD is used as a double pass and the IP1 pupil size is set to $2w$. Here, the y-direction corresponds to the direction along the ion chain, and w is the waist of the addressing/probe beam. Noise level refers to the maximum background intensity when the addressing/probe beam is turned off. 60

4.11 1. FP2 iris is set to a diameter of 10 mm, i.e., maximum Fourier plane aperture and 2. FP2 iris is set to 7 mm (1.a, 1.b, 2.a, 2.b) HDR images taken for varying pupil size $1.5w \leq d \leq 20w$. (1.c, 2.c) Corresponding effective aperture (d') for different pupil sizes (d). Here, the y-direction corresponds to the direction along the ion chain, and w is the waist of the addressing/probe beam. Noise level refers to the maximum background intensity when the addressing/probe beam is turned off. 61

4.12 Comparison of effective aperture ($d'(w)$) for different sizes of IP1 pupil ($d(w)$) for FP2 apertures of 7 mm and 10 mm, respectively. A linear decrease in the effective aperture ($d'(w)$) can be seen with a decrease in IP1 pupil sizes ($d(w)$). 63

4.13 (a) Shot-to-shot intensity fluctuation in the HDR images taken for a single data (b) Plot showing maximum (peak-to-peak) fluctuation and standard error at each point. Maximum peak-to-peak fluctuation is 4 dB, and maximum standard error is 1 dB. 64

List of Tables

2.1 Comparison of DMD and LC-SLM. 21

4.1 Average effective aperture $d'(w)$ for different FP2 apertures 62

List of Abbreviations

AQM Accidental Quantum Measurement 7–9, 11–13, 15, 17, 18, 28

DMD Digital Micromirror Device 6, 9, 16, 18, 20, 21, 29, 33, 34, 49

HDR High Dynamic Range 29, 36, 38, 41, 45, 56, 63

IFTA Iterative-Fourier Transform Algorithm 7, 9, 17, 23, 24, 28, 30, 48, 65

MCMR Mid-circuit Measurement and Reset 1, 2, 6, 7, 19, 27, 48, 65, 66

MWPM minimum weight perfect matching 9

NISQ Noisy Intermediate Scale Quantum 1

PMTs photomultiplier tubes 11, 17

QEC Quantum Error Correction 1

SNSPD Superconducting nanowire single-photon detector 11, 17

Chapter 1

Introduction

In the last two decades, committed efforts have been devoted by physicists, engineers, and mathematicians to push the frontiers of quantum technology. Many classically intractable problems, such as factorization of large prime numbers [1], performing molecular dynamics [2, 3], solving a large system of linear equations [4], and modeling protein folding [5], are expected to become tractable with the advent of quantum computing. While several theoretical breakthroughs, such as Shor's and Grover's algorithms [1, 6], have demonstrated the potential for quantum advantage, the development of large-scale quantum devices remains a significant challenge due to decoherence from environmental noise.

We are currently standing at the Noisy Intermediate Scale Quantum (NISQ) [7] era, where devices are not yet fully error-corrected but are still powerful enough to explore intermediate-scale quantum algorithms. These algorithms exploit the available resources, i.e., the partially error-corrected qubits, to tackle classically difficult problems [8]. The NISQ era devices aim to bridge the classical imperfections with the help of fault-tolerant quantum computers, which depend heavily on Quantum Error Correction (QEC). A critical component of QEC and of many near-term quantum algorithms is high-fidelity Mid-circuit Measurement and Reset (MCMR), which refers to performing a measurement or rest operation on a single isolated qubit within a quantum circuit or algorithm. This feature can introduce new capabilities to these devices, but also add complexity in the design and execution of quantum circuits.

Another promising and popular avenue that can be used to explore quantum mechanical systems is quantum simulators. In the words of Richard Feynman, quantum simulators are computers that are built on the principles of quantum mechanics that can mimic natural phenomena, precisely because nature itself is fundamentally quantum mechanical

[9]. A quantum simulator should have the ability to initialize a system, evolve the system under certain conditions, and perform measurements. Although quantum simulators do not directly rely on MCMR for their basic functionality, having this feature could expand their ability to simulate new areas in physics, such as measurement-induced quantum phase transitions [10, 11].

Many popular platforms have been explored to create a viable quantum computer or simulator. These include superconducting circuits [12, 13], photonic circuits [14, 15], neutral atoms [16], NV centers in diamonds [17], and trapped ions [18, 19]. Out of these, trapped-ion systems stand apart due to long coherence times of the qubits [20], easy state preparation and measurement procedures, and all-to-all connectivity, thus making them a suitable platform for both digital and analog quantum computation. Our group has been developing trapped-ion quantum simulators, which involve complex engineering since they rely on vacuum chambers, radio frequency (RF) engineering, and precision laser delivery. The first-generation trapped-ion quantum simulator developed by our team is the Amethyst processor. Some of the existing results obtained with this system have been referenced in the subsequent sections of this thesis. Currently, we are developing a larger-scale trapped-ion quantum simulator, the Bloodstone processor, which is described in more detail in Subsection 1.1.1.

1.1 Trapped-Ion Quantum Simulator

The first step towards making a trapped-ion quantum simulator is choosing the ion that acts as the qubit. We use $^{171}Yb^{+}$ as our atomic source due to its convenient hyperfine structure. An atomic oven is used to create an atomic flux, which is subject to photoionization. Neutral ^{171}Yb atoms go through a two step ionization process to create $^{171}Yb^{+}$. The first step involves isotope selection of Yb, which is done using a 399 nm laser, and then in the next step, the atom is further ionized by exciting the electron to the continuum using a 369 nm or 355 nm laser.

Subsequently, the ion needs to be trapped in a suitable trap geometry. Earnshaw's theorem [23] suggests that it is impossible to use a static electric field to trap a charged particle; hence, we use RF Paul traps [24]. These traps use an oscillating electric field, which creates a confining radial potential, and a constant axial voltage is applied for axial confinement. The effective confining potential is given by,

$$\phi_{\text{eff}} = \frac{1}{2}(\omega_x^2 x^2 + \omega_y^2 y^2 + \omega_z^2 z^2), \tag{1.1}$$

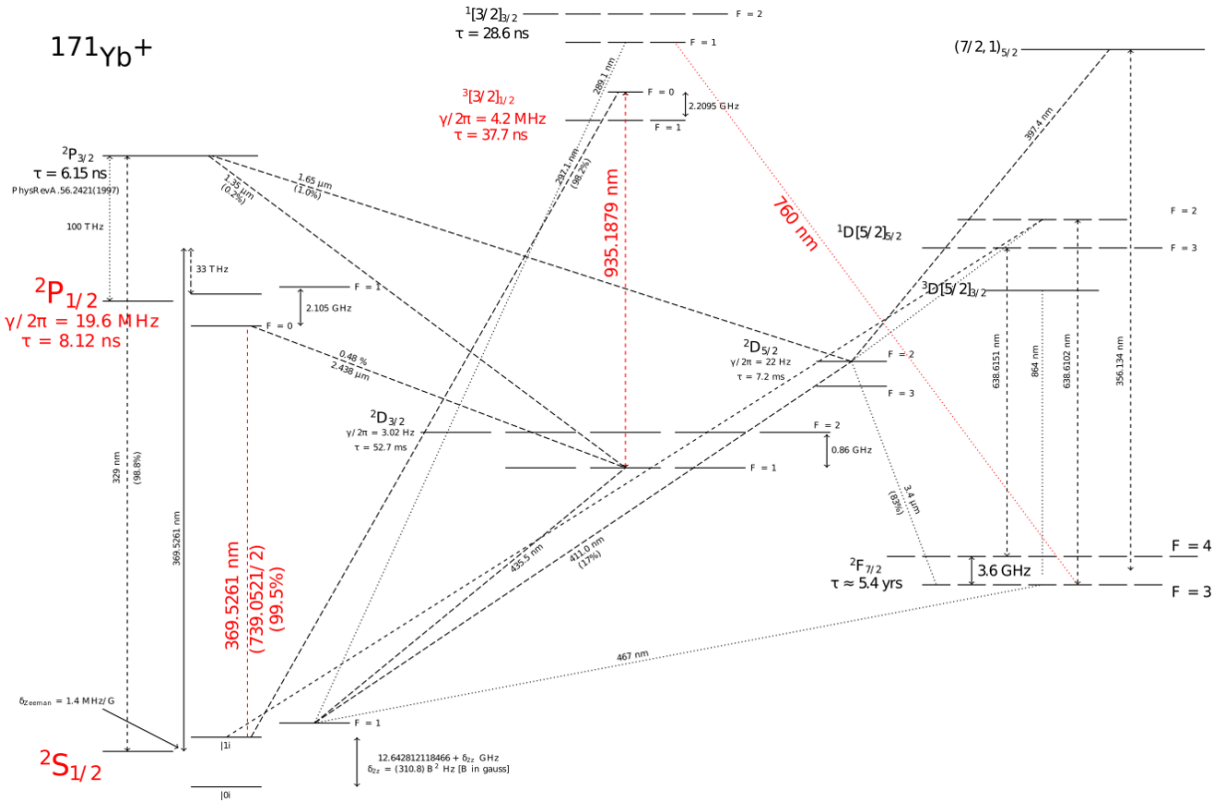


Figure 1.1: Energy level diagram for $^{171}Yb^{+}$. Relevant transitions and numbers are shown in red [21].

where ω_x and ω_y are the radial frequencies and ω_z is the axial frequency. This is also known as the pondermotive potential. Since we trap a linear chain of ions, our radial frequencies are much higher than the axial frequency, i.e., $\omega_x \approx \omega_y \gg \omega_z$. The ideal equilibrium position for the ion is at the RF null, but displacement from the static electric fields may shift the ion from the RF null location, which can induce micromotion of the ions. This micromotion causes heating and is a source of decoherence and needs to be minimized, which is done by adding compensating voltages to the RF electrodes.

Once trapped, the ions are cooled to their lowest energy state and initialized to the ground state using optical pumping. We use the hyperfine levels of the $^2S_{1/2}$ manifold of $^{171}Yb^{+}$ to encode the qubit states.

Manipulation of qubit states ($|\uparrow\rangle$ and $|\downarrow\rangle$ as shown in Figure 1.3) can be done using single-qubit rotations and entangling gates. Since the transition between the $|\uparrow\rangle$ and $|\downarrow\rangle$

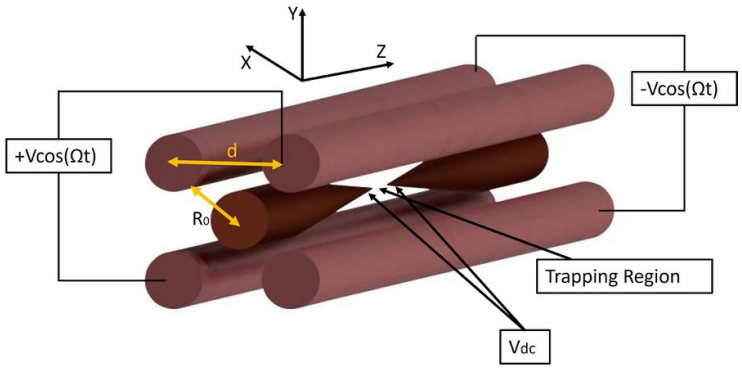


Figure 1.2: Figure showing a four-rod Paul trap where the four parallel rods are supplied with oscillating voltages $\pm V\cos(\Omega t)$ and a constant DC voltage is supplied to the end caps [22].

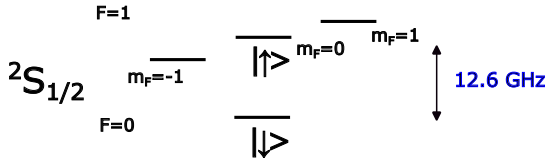


Figure 1.3: Qubit states, $|\uparrow\rangle$ and $|\downarrow\rangle$ represented by ${}^2S_{1/2}\,|F=1, m_F=0\rangle$ state and ${}^2S_{1/2}\,|F=0, m_F=0\rangle$ state, respectively. The qubit frequency is given by $2\pi \times 12.6$ GHz.

is a microwave transition ($2\pi \times 12.6$ GHz), we can use a microwave source to drive Rabi oscillations between the qubit states. However, the long wavelength corresponding to the transition makes it difficult to generate spin-motion coupling, which is essential for generating an entangling gate; hence, the microwave transition serves as a global operation. We can also use stimulated Raman transitions to drive single-qubit rotations, where two far-detuned Raman beams (355 nm) are used to drive a Rabi oscillation by matching their beatnote frequency with the qubit frequency. Entangling operations are done by following the Mølmer Sørensen scheme [25], which relies on generating a spin-motion coupling from the stimulated Raman transitions. This is done by setting a symmetric detuning to the red sideband (RSB) and the blue sideband (BSB) transitions with different phases.

1.1.1 Bloodstone Processor

Progress has been made towards developing a brand new trapped-ion quantum simulator, the Bloodstone processor, through the combined efforts of the previous generation and

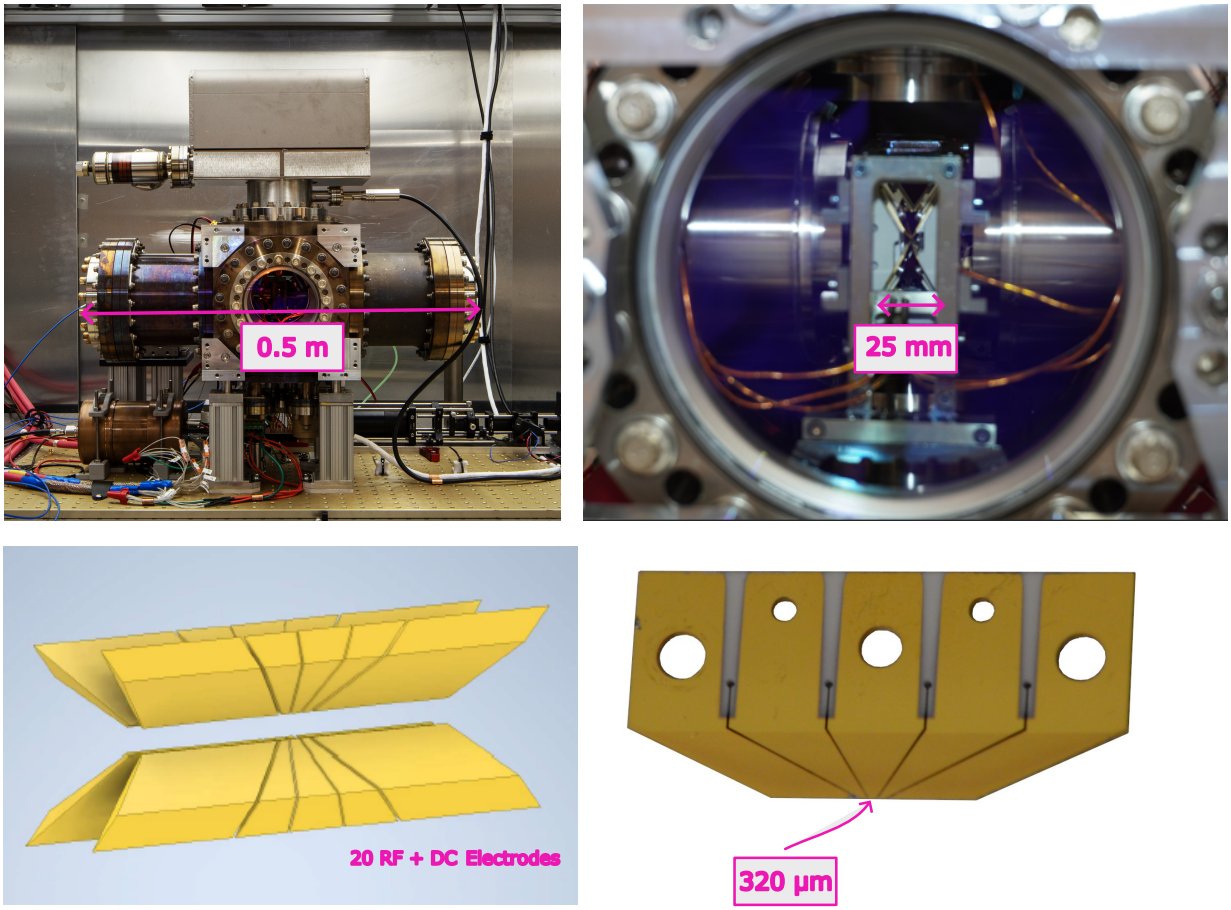


Figure 1.4: Top left shows the vacuum chamber, which houses the ion trap. Top right shows the cross-section of the blades as seen from the front of the chamber. Bottom left shows a CAD model of the segmented blades, which serve as the electrodes. Bottom right shows a single blade where the marked central segment serves as the main trapping region.

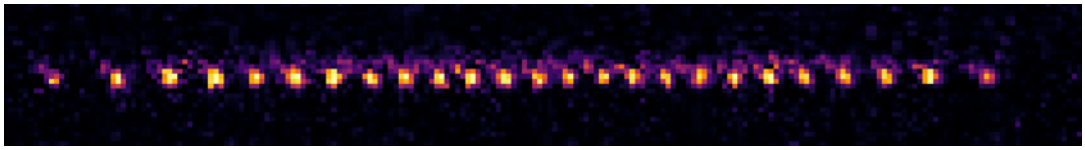


Figure 1.5: Fluorescence observed from a chain of 25 $^{171}Yb^{+}$ ions trapped in the Bloodstone processor when illuminated with a 369 nm laser beam corresponding to the transition $^{2}S_{1/2} \rightarrow {}^{2}P_{1/2}$

the present generation of the group. The Bloodstone processor is based on a segmented blade trap geometry, which gives added control over the ions and a higher optical access. The system is designed to accommodate > 30 ions. The high optical access will facilitate addressing of individual ions with high precision, which will enable us to do in-situ MCMR. The work presented in this thesis discusses the engineering of this addressing beam with improved intensity crosstalk compared to what was achieved previously [26]. More detailed descriptions about the design and assembly of the trap can be found in Ref. [21, 27].

1.2 Thesis Overview

The following outline provides a guide to the content of the thesis:

- In Chapter 2, I give a brief overview of the research problem, describe the existing technique used for engineering the individual addressing beam, and introduce the methods developed to improve the existing results.
- In Chapter 3, I introduce one of the proposed techniques, the secondary grating method, and present experimental results demonstrating a reduction in the absolute intensity crosstalk at the nearest neighbor up to the intermediate image plane.
- In Chapter 4, I introduce the second proposed method, using the Digital Micromirror Device (DMD) in a double-pass configuration, which targets the reduction of intensity crosstalk at the asymptotic limit further away along the ion chain.
- In Chapter 5, I summarize the results and provide an outlook on how incorporating these methods into the engineering of a low-crosstalk individual addressing beam can improve the fidelity of MCMR operations in a trapped-ion system.

Chapter 2

Engineering a low-crosstalk individual addressing beam

This chapter discusses the motivation behind my master's thesis project and provides a comprehensive overview of the theoretical background. The methods discussed in this chapter related to employing an amplitude grating for hologram generation, Iterative-Fourier Transform Algorithm (IFTA), and the method of aberration compensation have been adopted from previous research conducted by Dr. Chung-You (Gilbert) Shih. The methods established to characterize Accidental Quantum Measurement (AQM) and inter-ion scattering have been adopted from previous research conducted by Dr. Sainath Motlakunta.

2.1 Overview

An important feature that opens up several capabilities in a quantum simulator is the ability to perform MCMR operations. A typical flow of a quantum circuit consists of several single-qubit and two-qubit gates followed by a global measurement at the end of the circuit. The ability to perform a measurement or reset operation on a single isolated qubit within a quantum circuit or an algorithm is known as MCMR. This feature expands the capabilities of a quantum simulator to perform experiments such as measurement-induced quantum phase transitions [10, 11], reservoir engineering with controlled dissipation [28], execution of quantum error correction protocols [29], and circuit optimization with qubit-reuse [30].

The dissipative nature of MCMR makes it a challenging problem in trapped-ion qubits, hence, efforts are made to isolate the data qubits or asset qubits (qubits not meant to be

measured) from the auxiliary qubits or process qubits (qubits required to be measured) during the process. Several techniques have been suggested to perform MCMR in atomic systems. These include using different atomic species for auxiliary qubits [31, 32, 33], shuttling ions in and out of measurement/reset zones [34, 35, 36], shelving ions to a different energy level and thus hiding the data qubits from the measurement/reset atomic transition [37, 38] and adding micromotion to data qubits to hide them from the resonant frequency of the corresponding atomic transition [39, 40]. Shuttling of ions requires special kinds of traps, such as surface traps, which are equipped with hundreds of electrodes. These traps deal with significant challenges in terms of motional heating, anharmonicity in trapping potential, and shallow trap depths [41, 42, 43]. Hence, we have adopted a trap architecture that prioritizes larger trapping depth and more harmonic trapping potential, making it more suitable for large-scale quantum simulations. Our choice of trap architecture makes our system incompatible with allowing the shuttling of ions and the use of multi-species atomic sources, which is also dependent on shuttling to allow reordering of qubits. The other techniques increase experimental complexity and can still suffer from long-range measurement errors introduced by a less efficient probe beam, as observed in Ref. [40]. Hence, our group has adopted a bolder approach, utilizing spatial modification of light to create a crosstalk-free addressing beam [26, 44]. This approach can also be combined with other MCMR architectures to achieve even higher MCMR fidelities.

Most trapped-ion systems are equipped with global laser beams designed to perform simultaneous global detection and reset on all qubits. MCMR demands both precise spatial modification of the addressing beam and an efficient imaging system with improved photon-collection efficiency for faster measurements. Since MCMR is a dissipative operation, careful engineering of the addressing beam with reduced probability of AQM, i.e., accidentally measuring an asset qubit while addressing a process qubit [44] paves the way towards a fault-tolerant scheme.

Our group has been using Fourier holography [26] to optically engineer the individual addressing beams, which are meant to perform the in-situ MCMR operations. The results presented in this thesis demonstrate a more robust engineering of the individually addressing beam with capabilities to reduce the absolute intensity crosstalk at the nearest neighbor qubit to $45 - 50$ dB, i.e., ≈ 6 dB lower than the intensity crosstalk obtained previously [26] and below 60 dB (limited by the background noise floor) intensity crosstalk at the asymptotic limit which is reached beyond the third nearest neighbor qubit. This work can potentially improve the existing state-of-the-art preservation fidelities of the asset qubit for measurement and reset operations on the process qubit, i.e., 99.6% and 99.9%, respectively [44].

Achieving high-fidelity MCMR is essential for implementing quantum error correction

protocols. For instance, a typical surface code using a minimum weight perfect matching (MWPM) decoder requires the measurement error rate to be below 0.57% [45]. Since error correction involves multiple cycles of MCMR, improving measurement and reset fidelities is crucial for approaching a fully error-corrected system.

The optical engineering improvements to the addressing beam proposed in this thesis may contribute to higher mid-circuit measurement and reset fidelities, thereby advancing the development of a fault-tolerant quantum computing architecture.

2.1.1 Chapter Outline

The chapter outline is given as follows:

- In Section 2.2, I discuss the physics involved in the state detection and reset processes in $^{171}Yb^{+}$.
- In Section 2.3, I review the challenges involved in engineering a low-crosstalk individual addressing beam. I discuss the various sources of decoherence/crosstalk that can cause AQM.
- In Section 2.4, I review the previous results obtained using Fourier holography and motivate the requirements for the improvements suggested in the thesis.
- In Section 2.5, I give a background on how the Fourier holography technique has been used to engineer our addressing beam with the help of a Digital Micromirror Device (DMD) and discuss IFTA, the method used in Ref. [26] to build the current state-of-the-art individual addressing system.
- In Section 2.6, I discuss the procedure for extracting the aberration map in the optical system.

2.2 State Detection and Reset in $^{171}Yb^{+}$

State detection and state reset are important attributes in a trapped-ion quantum simulator. State detection helps to identify the qubit state of an ion, and state reset helps to re-initialize the ion to the ground state. The following subsections describe the physics involved in state detection and state reset processes in $^{171}Yb^{+}$.

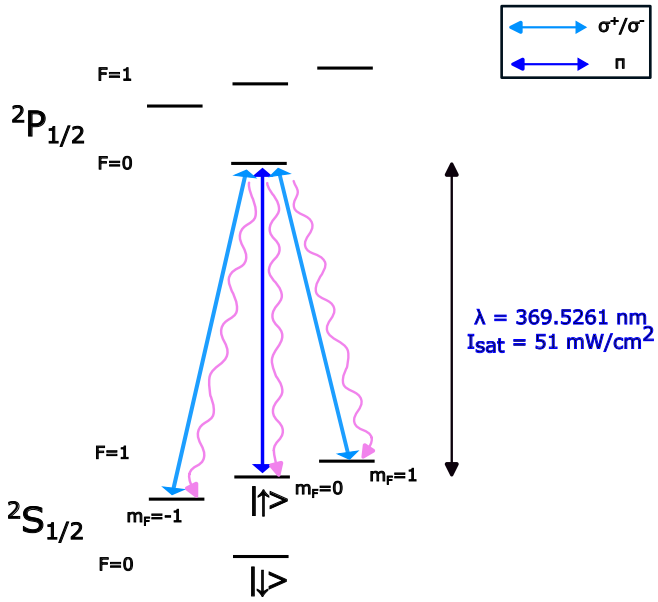


Figure 2.1: Schematic representation of state detection procedure in $^{171}Yb^{+}$.

2.2.1 State Detection

State detection is the process of identifying the qubit state of an ion, which is encoded as either $|\uparrow\rangle$ or $|\downarrow\rangle$. This encoding is done in $^{171}Yb^{+}$ ions using the hyperfine levels of the $^2S_{1/2}$ manifold as described in Chapter 1. Determination of the encoded state of the ion is done by illuminating it with light resonant to the transition $^2S_{1/2}\,|F=1\rangle \rightarrow {}^2P_{1/2}\,|F=0\rangle$ as shown in Figure 2.1. On shining an ion in qubit state $|\uparrow\rangle$ with the detection light, it gets excited to the $^2P_{1/2}\,|F=0\rangle$ and spontaneously emits photons as it decays back to $^2S_{1/2}\,|F=1\rangle$ (transition to $^2S_{1/2}\,|F=0\rangle$ is forbidden). The fluorescence from the spontaneous emission is detected by a detector, and hence the state of the ion is inferred to be $|\uparrow\rangle$. The detection light does not excite an ion in qubit state $|\downarrow\rangle$ and therefore there is no fluorescence. Since the detector does not detect any photon, the qubit state of the ion is inferred to be $|\downarrow\rangle$.

The transition $^2S_{1/2}\,|F=1\rangle \rightarrow {}^2P_{1/2}\,|F=0\rangle$ is nearly closed with $< 0.5\%$ decay probability to the $^2D_{3/2}$ state. In order to make the transition continually cyclic, a repump laser beam corresponding to wavelength 935 nm is used to excite the ion in the $^2D_{3/2}$ state to the $^3[3/2]_{1/2}$ state, which subsequently decays to the $^2S_{1/2}$ state. Due to the cyclic transition, the $|\uparrow\rangle$ state keeps getting excited to $^2P_{1/2}\,|F=0\rangle$ and undergoes spontaneous emission for the entire time the detection light is turned on, also known as the detection time, while $|\downarrow\rangle$ remains dark. The duration of the detection time is determined by the state detection

protocol being used and is often limited by the photon collection efficiency of the imaging system. Additionally, background scattering and detector noise require a sufficiently high detection time to collect an adequate amount of signal. While longer detection time ensures good confidence in the process ion's qubit state, it can increase the probability of AQM of the asset ions. High fidelity state detection techniques have enabled really short detection times of 11 μs using a Superconducting nanowire single-photon detector (SNSPD), which has significantly higher (almost double) efficiency in detecting photons as compared to photomultiplier tubes (PMTs) [46]. In the Bloodstone Processor, a detection technique using PMTs has been developed and is estimated to have comparable detection time in the order of 20 μs [47], which is the time needed to scatter enough photons (≈ 100) to detect a single photon on the PMT (limited by the collection efficiency of the imaging system).

During the decay process from ${}^2P_{1/2}\,|F=0\rangle$ state, the ion can decay to one of the following energy states, ${}^2S_{1/2}\,|F=1, m_F=\pm 1\rangle$ or ${}^2S_{1/2}\,|F=1, m_F=0\rangle$ where the $|\uparrow\rangle$ state corresponds to ${}^2S_{1/2}\,|F=1, m_F=0\rangle$. A mixed polarization with equal proportions of $\sigma_\pm$ and π ensures that the excitation and emission processes continue.

Even with a mixed polarization for the detection light, there is a probability that the ion in $|\uparrow\rangle$ state decays to a coherent dark state. In that case, it will no longer continue to be in the cyclic transition. This effect can reduce the fidelity of detection. However, this effect can be conveniently minimized by breaking the degeneracy of the Zeeman levels in the ${}^2S_{1/2}\,|F=1\rangle$ manifold by applying a magnetic field which introduces a Zeeman shift in the m_F levels. Other processes, such as off-resonant excitation and dark state pumping, can also impact the fidelity of detection, but with low probability.

2.2.2 State Reset

State reset, also known as optical pumping, is used to re-initialize the state of the qubit to the ground state $|\downarrow\rangle$. This is done by shining the ion with the optical pumping light, which is resonant to the transition ${}^2S_{1/2}\,|F=1\rangle \rightarrow {}^2P_{1/2}\,|F=1\rangle$ as shown in Figure 2.2. The optical pumping light excites the ion in qubit state $|\uparrow\rangle$ to ${}^2P_{1/2}\,|F=1\rangle$ state which decays back to either ${}^2S_{1/2}\,|F=1\rangle$ or to ${}^2S_{1/2}\,|F=0\rangle$, i.e. $|\downarrow\rangle$. Eventually, the ion decays to the ground state, $|\downarrow\rangle$, on repeating the process multiple times. For an ion in qubit state $|\downarrow\rangle$, the ion does not undergo any excitation due to the optical pumping light and remains in the same qubit state. Mixed polarization consisting of $\sigma_\pm$ and π is also required during optical pumping to ensure the energy state of the ion is not stuck at ${}^2S_{1/2}\,|F=1, m_F=\pm 1\rangle$.

The probability of $|\uparrow\rangle$ resetting to $|\downarrow\rangle$ increases with the increase in the duration the

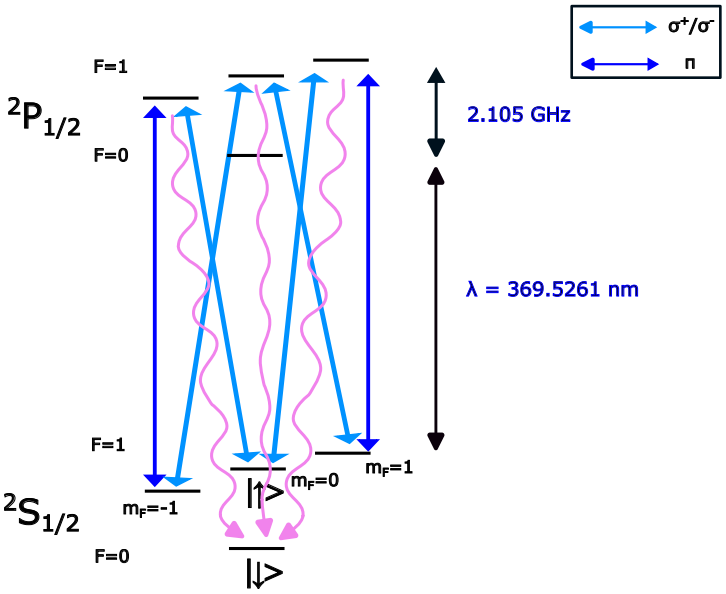


Figure 2.2: Schematic representation of state reset procedure in $^{171}Yb^{+}$.

optical pumping beam is turned on. An exponential decay curve is obtained from the scattered photon counts as the $|\uparrow\rangle$ decays to $|\downarrow\rangle$ with the duration of illumination of the optical pumping beam. The characteristic of this exponential decay curve is also dependent on the power and polarization of the optical pumping beam. The optical pumping time is determined from this decay curve, such that the qubit state of the ion is reset to $|\downarrow\rangle$ with a probability greater than 99.9%. Unlike the state detection process, which relies on the collection efficiency of the imaging system and the sensitivity of the detector, the state reset process is faster because only a few scattered photons are sufficient to reset the qubit state of an ion. In our experiments, the optical pumping time ranges between $1 - 10$ μs.

2.3 Sources of error

Engineering an individual addressing beam is a challenging problem since leaked light scattered from the addressing beam has enough photons to destroy the qubit states of the neighboring ions. For convention, I will be referring to the ion being addressed as the process qubit (ion 2) and the ion to be preserved as the asset qubit (ion 1). The probability that an asset qubit is accidentally measured while addressing a process qubit, also known as accidental quantum measurement (AQM) [44] can be attributed to two main

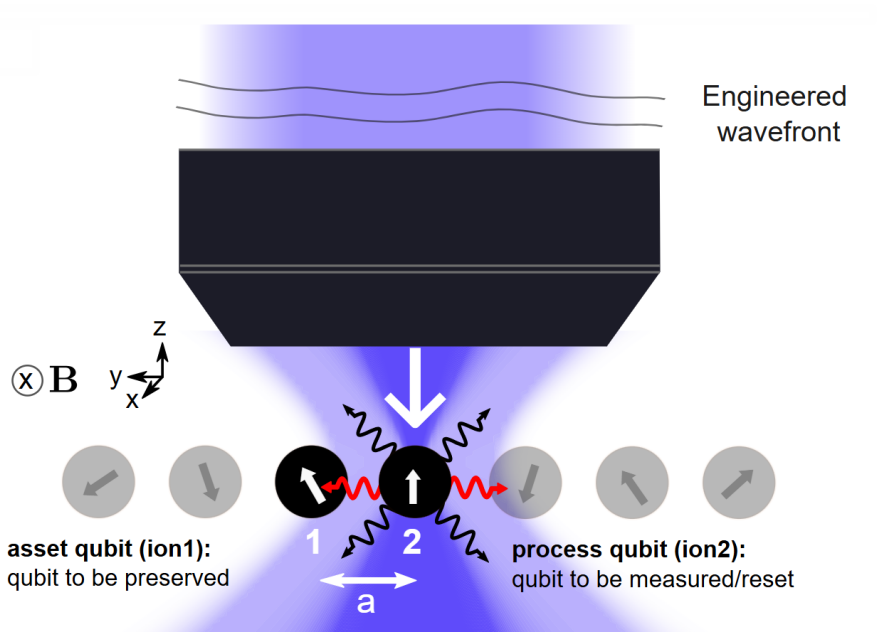


Figure 2.3: Demonstration of AQM. Here, ion 2 is the process qubit, which is being addressed, and ion 1 is the asset qubit, which we would like to preserve. The figure demonstrates the two sources of AQM as discussed in Section 2.3. This figure has been adapted from [44].

reasons: 1. an imperfect addressing beam, where there is some finite intensity crosstalk at the neighboring ion location and/or 2. inter-ion scattering, where a photon scattered from the process qubit gets absorbed by the asset qubit. State detection processes require a higher number of scattered photons as compared to the state reset process due to the limited efficiency of detection systems (a few percent). Hence, the chances of AQM from state detection are higher than from the state reset process. The following subsections provide a brief overview of each source of error, along with its dependencies and estimated magnitude.

2.3.1 Finite intensity crosstalk

Engineering an addressing beam is particularly challenging when the ion-to-ion separation is small (typically a few microns). Our target quantum simulation experiments with the Bloodstone Processor require the ions to be separated by 4 μm. Hence, the probability that a leaked photon from the addressing beam gets absorbed by an asset qubit can be

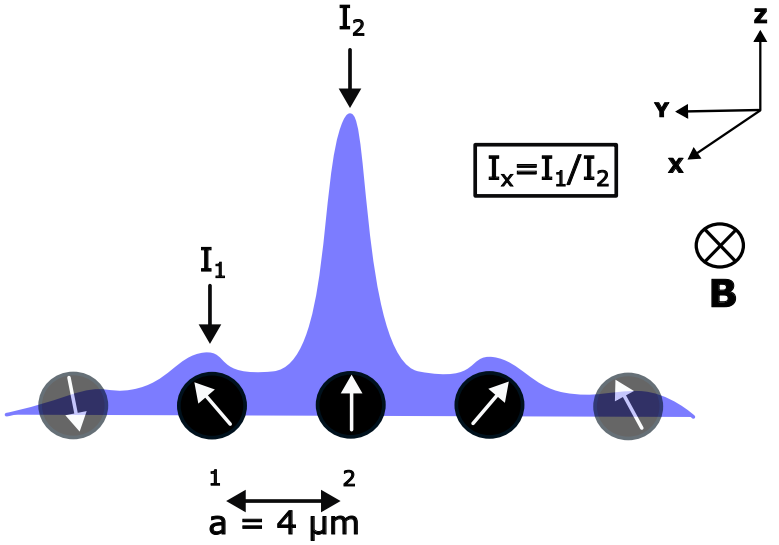


Figure 2.4: Figure demonstrating an imperfect addressing beam with some finite intensity crosstalk at ion 1 or the asset qubit. I_X defines the relative intensity crosstalk between ion 2 and ion 1. The magnetic field direction is perpendicular to the ion-chain as well as the direction of the addressing beam.

high.

Intensity crosstalk refers to the intensity of light falling on the asset qubit relative to the intensity of light falling on the process qubit when addressing the process qubit with a uniform Gaussian beam. If the intensity of light falling on the asset qubit is given by I_1 and the intensity of light falling on the process qubit is given by I_2, the intensity crosstalk (I_X) is defined as $I_X = I_1/I_2$.

The net scattering rate for an ion when illuminated with light of intensity I for a two-level system is given using the following formula,

$$R_{\text{sc}} = \frac{\Gamma}{2} \frac{I/I_{\text{sat}}}{1 + 4(\Delta/\Gamma)^2 + I/I_{\text{sat}}}, \tag{2.1}$$

where R_{sc} is the net scattering rate, Γ is the linewidth of the $^2P_{1/2}$ state given by $2\pi \times 19.6$ MHz, I is the intensity of the illuminating light, I_{sat} is the saturation intensity given by 51 mW/cm^2 ($I_{\text{sat}} = \frac{\pi hc}{3\lambda^3\tau}$; here, λ is the wavelength of the relevant transition and τ is the lifetime of the excited state) and Δ is the detuning from the resonant frequency for the transition.

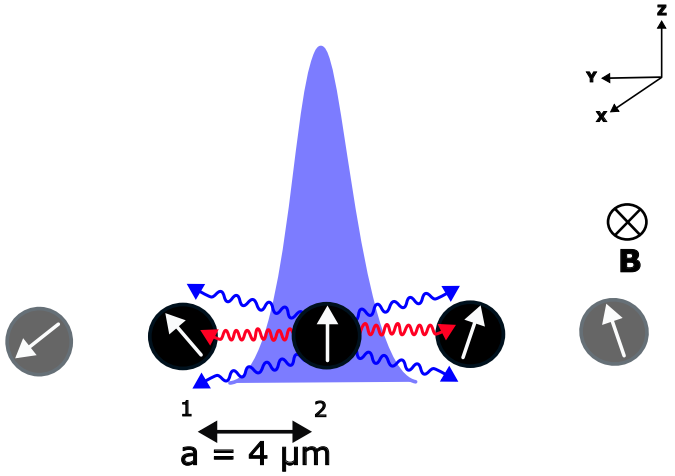


Figure 2.5: Figure demonstrating inter-ion scattering (red) under the conditions of a perfect addressing beam with no intensity crosstalk, I_X at ion 1.

For detection, $\Delta \approx 0$ and $I_2 = I_{\text{sat}}$, hence the scattering rate for the asset ion is proportional to the intensity crosstalk, $R_{\text{sc},1} \propto I_X$ when $I_X \to 0$ (usually $I_1 \ll I_2$). Thus, the total number of photons scattered can be given as,

$$n_{\text{photons}} = R_{\text{sc},1} \times \tau_{\text{det}}.$$

Therefore,

$$n_{\text{photons}} \propto I_X \times \tau_{\text{det}}, \tag{2.2}$$

where τ_{det} is fixed based on the state measurement protocol being used for the detection process and the efficiency of the detector being used. Therefore, the probability of AQM of the asset ion is directly related to the absolute value of the intensity crosstalk (I_X) at the asset ion. The existing techniques (discussed in more detail in Section 2.4) have been able to achieve an intensity crosstalk, I_X, in the order of 10^{-4}.

2.3.2 Inter-ion scattering

The AQM of the asset ion due to inter-ion scattering is caused by the absorption of π polarized photons scattered from the process ion when illuminated with detection light. The scattering rate will thus depend on the separation of the two ions as well as the direction of the magnetic field. Under perfect conditions where the addressing beam does

not introduce any crosstalk at the asset ion, the probability of absorbing a scattered photon from the process ion is given by [44],

$$I_{\text{ab},1} = f_{\text{pol}} f_{\text{angle}} \frac{h\nu R_{\text{sc},2}}{4\pi a^2}, \tag{2.3}$$

where f_{pol} represents the fraction of light with the appropriate polarization that affects ion 1, f_{angle} is the angular dependence of the polarization of the scattered light to the magnetic field direction, ν is the frequency of transition, a is the ion-to-ion separation, and $R_{\text{sc},2}$ is the scattering rate of ion 2 or the process qubit.

When addressing the ion 2, the ion 2 scatters photons of all polarizations. Since the ions are initialized to $m_F = 0$, AQM of ion 1 will be caused when it absorbs π polarized photons; hence, $f_{\text{pol}} = 1/3$. The direction of the magnetic field in the system sets the direction of the π polarization in the scattered light; hence, the angular dependence is given by,

$$f_{\text{angle}} = \sin^2\theta, \tag{2.4}$$

where θ is the angle between the direction of the magnetic field and the ion-chain.

In our experiment, the direction of the magnetic field is perpendicular to the ion chain; hence, $\theta = \frac{\pi}{2} \implies f_{\text{angle}} = 1$. $R_{\text{sc},2}$ can be calculated using Equation 2.1 with $I = I_{\text{sat}}$. Assuming ion-to-ion separation, $a = 4$ μm, we can estimate $I_{\text{ab},1} \approx 2.14 \times 10^{-5} I_{\text{sat}}$ for a state detection process.

For state reset, the polarization dependence changes, since now the ion 1 can absorb either σ^+ or σ^-, hence, $f_{\text{pol}} = 2/3$. The polarization dependence sets $f_{\text{angle}} = 1/2$ [44]. This gives us an estimate, $I_{\text{ab},1} \approx 2.92 \times 10^{-6} I_{\text{sat}}$ for a state reset process.

Since inter-ion scattering is inevitable during addressing the process qubit either for a state detection or a state reset process, $I_{\text{ab},1}$ sets a fundamental limit to the crosstalk introduced at the asset qubit while individually addressing the process qubit using a probe beam. These sources of error motivate the techniques mentioned in the upcoming Section 2.4 to mitigate the crosstalk errors introduced by the individually addressing beam.

2.4 Existing techniques

References [26, 44] employ a Fourier holography technique (discussed in Section 2.5), aided by a Digital Micromirror Device (DMD), to engineer an incoming wavefront to generate the individual addressing beam. This technique not only allows for precise engineering of the

addressing beam but also offers the added advantage of in-situ aberration compensation. The binary nature of the DMD requires the binarization of the continuous DMD hologram. A deterministic algorithm, IFTA, is used to mitigate the binarization errors introduced in the target electric field at the image plane. This helps to reduce the artifacts arising from binarization at the image plane within a defined signal window. A spatial filter introduced at the intermediate image plane can help to block the erroneous signal outside the signal window.

This method has been used to create the current state-of-the-art individual addressing system with intensity crosstalk I_X value (See Section 2.3.1) below 10^{-4} [26], considering an ion-to-ion spacing of 6 μm. This intensity crosstalk of $I_X < 10^{-4}$ is maintained across the ion chain (> 400 μm, suitable to address > 50 ions). Using the same architecture, Ref. [44] employs a clever method of characterizing the crosstalk, which is more robust against unwanted background scattering with the help of Ramsey interferometry. The fidelity of preserving an asset qubit is computed from the decoherence time, T_2^*, of the asset qubit after a reset or measurement operation is done on the process qubit and is given by,

$$F_{1|2} = \frac{2}{3}\exp[-\frac{\tau(\text{ion2})}{T_2^*(\text{ion1})}] + \frac{1}{3}, \tag{2.5}$$

where τ(ion2) is the time for which the process qubit is illuminated with the addressing beam and P_{AQM} is characterized as the infidelity under the assumption $P_{\text{AQM}} \ll 1$ and long coherence (> 200 ms) of asset qubits in the absence of probe beam.

Using this method, it was shown that the probability of AQM is: $P_{\text{AQM}} < 1 \times 10^{-3}$ for for individual state reset and $P_{\text{AQM}} < 4 \times 10^{-3}$ for individual state detection (when turned on for 11 μs) which also corresponds to a preservation fidelity of 99.9% and 99.6%, respectively.

2.4.1 Scope of Improvement

Error correction codes typically have multiple cycles of measurement. Thus, improving the total measurement error, which contributes to the physical error of the qubits, can help improve the logical error rates in these error correction codes. This will have implications in reducing the distance of error correcting codes, i.e., the number of physical qubits encoded as a logical qubit, thus decreasing net resource cost. Previously obtained fidelity values meet the error threshold requirement 0.5% for most of the popular error correction codes, but are constrained to 11 μs detection times, which requires sophisticated detection techniques using SNSPD [46]. PMTs require longer detection times, hence to maintain the

same error rate, i.e., $P_{AQM} < 0.5\%$, I_X has to be improved. Thus, the results mentioned in this thesis suggest two areas for improvement: 1. The absolute value of I_X at the nearest neighbor, and 2. The asymptotic value of I_X for mitigating long-range measurement error further away from the process qubit.

Absolute intensity crosstalk (I_X)

The Gaussian distribution of intensity profile for the image plane beam leads to higher crosstalk at the nearest neighbor as compared to distant ions, when compared in absolute terms. Hence, the proximity of the nearest neighbor makes it more susceptible to AQM. The waist of the addressing beam in the results mentioned above is $w = 1.5$ μm and the ion-to-ion separation is $4 \times w = 6$ μm. The minimum achievable intensity crosstalk, I_X, at the nearest neighbor is fundamentally limited by inter-ion scattering, which is $\approx 10^{-5}$ for the detection beam at an ion-to-ion separation of 4 μm. This leaves room for further improvements in our addressing beam to approach this fundamental limit.

To address this, I suggest a secondary grating method (See Chapter 3). This method utilizes a small portion of the Fourier plane to create a secondary beam at the neighboring ion location. It relies on creating a local destructive interference at the neighboring ion location, thereby canceling out the I_X from the primary addressing beam by controlling the amplitude and phase of the secondary beam. This method has shown promising results by reducing the absolute value of crosstalk (I_X) at the nearest neighbor by 6 dB, measured using a camera.

Long-range measurement error

In the results mentioned above (Section 2.4), I_X decreases as we move away from the center of the probe beam, and saturates at 10^{-4} after a point in the ion chain (> 50 ions). This might lead to a constant propagation of errors in a long chain of ions. An intensity crosstalk of $I_X = 10^{-4}$ corresponds to the probability of measurement error, $P_{AQM} < 4 \times 10^{-3}$. Thus, for a chain of 10 ions, the cumulative error will be $10 \times 4 \times 10^{-3} = 4 \times 10^{-2}$, already making it an order of magnitude worse.

To address this, I use the DMD as a double pass (See Chapter 4) where the DMD interacts with the laser beam twice. In this method, one portion of the DMD acts as a Fourier hologram generator, and the other portion acts as an intermediate image plane pupil which further filters out the tail of the Gaussian beam, thus reducing the asymptotic value of I_X in the addressing beam. This has enabled a reduction in the intensity crosstalk

to as low as 10^{-6} or 60 dB, which was measured with a camera. This result will have a significant impact when mitigating long-range measurement errors, which is also an impending challenge in other MCMR architectures [40].

2.5 Fourier Holography with a DMD

2.5.1 Working principle

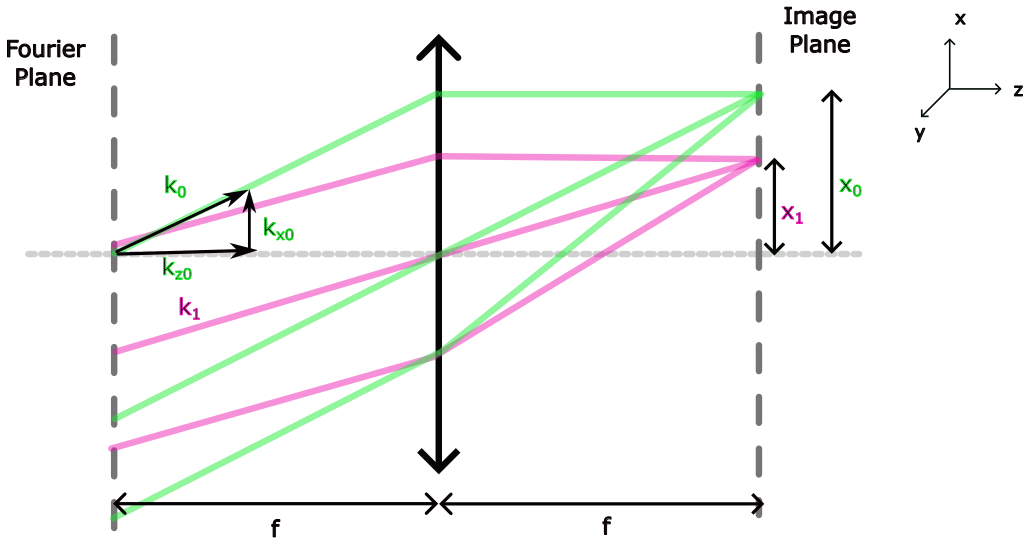


Figure 2.6: Figure showing the dependence of wave vector ($k_{i=0,1}$) at the FP with spatial position in IP ($x_{i=0,1}$). The electric field at the FP can be represented as a sum of infinite plane waves (k_i), each of which corresponds to different spatial locations (x_i) at the IP.

The existing techniques mentioned in Section 2.4 use Fourier holography to generate the addressing beam profile at the ion plane. Fourier holography exploits the idea that the lens acts as a Fourier transform between its back and front focal planes. For simplicity, I will refer to the front focal plane as the Fourier Plane (FP) and the back focal plane as the Image Plane (IP). Fourier holography with a lens can be visualized by breaking down the electric field at the Fourier plane into a sum of different plane waves (k_i) (as shown in Figure 2.6). Under paraxial approximation, each plane wave will correspond to a spatially separated diffraction-limited spot at the image plane (visualizing in 1 dimension for simplicity, $\delta(x - x_0)$). We can exploit the following geometric relationship between the

FP and IP (Figure 2.6),

$$\frac{k_{x0}}{k_{z0}} = \frac{x_0}{f}. \tag{2.6}$$

Assuming beam propagation axis along z, we can make a small angle approximation such as $k_0 \approx k_{z0}$. This gives us,

$$\frac{x_0}{f} = \frac{k_{x0}}{k_0} \implies x_0 = \frac{\lambda}{2\pi} f k_{x0}. \tag{2.7}$$

Thus, it can be seen that the coordinates at the FP and the IP are related as Fourier conjugates; hence, we can conclude that the electric field profiles at the two focal planes are Fourier conjugate pairs with some scaling factor. Thus, we have the following transformation [48],

$$E_{\mathrm{FP}}(x) e^{i\phi_{\mathrm{ab}}^{(\mathrm{IP})}(x)} = \frac{\lambda f}{2\pi} \mathcal{F}[E_{\mathrm{IP}}(x')](k') \Big|_{k'=\frac{2\pi}{\lambda f}x}, \tag{2.8}$$

where E_{FP} is the electric field at the FP, E_{IP} is the electric field at the IP, x' is the spatial coordinate at the IP, and k' is the wave vector at the FP.

This principle can be generalized to any electric field profile since it can be expressed as a sum of independent plane waves, and Fourier transform is linear. Under non-ideal conditions, the one-to-one mapping between the FP and IP is affected by the aberrations introduced by the lens. To model the aberrations in the system, we can construct a phase map at the FP given by $e^{i\phi_{\mathrm{ab}}^{(\mathrm{IP})}(x)}$. A detailed description of how the phase map is extracted can be obtained in Section 2.6.

Thus, a reprogrammable hologram can be placed at the FP to engineer an input waveform to generate any arbitrary beam profile at the IP. This can be done using commercially available adaptive optics such as deformable mirrors (DM), liquid-crystal spatial light modulators (LC-SLM), and DMD.

2.5.2 Reprogrammable Hologram with DMD

The choice of hardware for generating the reprogrammable hologram is dependent on two major factors: 1. optical efficiency of the hardware at the operating wavelength (UV), and 2. switching speed. Based on these factors, DMD and LC-SLM can be compared as in the Table 2.1.

	DMD	LC-SLM
Optical efficiency	There are commercially available DMDs which are meant for UV and can withstand high optical power (up to 10 Watts [48]) at UV.	They are more prone to solarization due to UV.
Switching speed	High switching speed (>10 kHz)	Low switching speed (<1 kHz)

Table 2.1: Comparison of DMD and LC-SLM.

Although DMDs have faster refresh rates with individual micro mirrors getting switched in the order of 10 μs, the delay in communication with the DMD controller is of the order of 100 μs. Hence, for quantum applications, an Acousto-Optic Modulator (AOM) is juxtaposed with a DMD to function as a high-speed switch, since it can operate at MHz rates. DMDs are binary, which means the individual mirrors can only switch between ON and OFF states, unlike LC-SLM, which has a continuous surface. To get a full phase control of the beam, an amplitude grating is employed as discussed in Subsection 2.5.3.

2.5.3 Amplitude grating and IFTA

Amplitude grating function

A DMD consists of a 2-dimensional micro mirror array, where each mirror can toggle between two angles, thus reflecting the light in two different directions. Thus, to use the DMD for optical phase modulation along with amplitude modulation, an amplitude carrier grating can be employed [48].

The DMD is divided into several super pixels where pixels are turned ON and OFF in a manner to give rise to alternating bright (ON state) and dark (OFF state) regions, which constitute the amplitude grating. Changing the spatial phase of the amplitude grating helps to control the phase of the diffracted beam; thus, the amplitude grating can be used for simultaneous phase and amplitude modulation of the diffracted beam. To understand the working of the carrier grating, I will follow the work mentioned in Dr. Chung-You (Gilbert) Shih's master's thesis (2019) [48]. For simplicity, let's assume a grayscale DMD where $f(\mathbf{x})$ is the target beam profile, then the corresponding Fourier conjugate is given

by,

$$F(\mathbf{k}) = \mathcal{F}[f(\mathbf{x})],$$

where $\mathbf{x} = (x, y)$ and $\mathbf{k} = (k_x, k_y)$.

For an ideal case, where the DMD is uniformly illuminated and there are no aberrations in the system, the grating function can be given as,

$$G(\mathbf{k}) = \frac{|F(\mathbf{k})|}{2}(\cos(\mathbf{x_0} \cdot \mathbf{k} + \Phi(\mathbf{k})) + 1), \tag{2.9}$$

where $|\mathbf{x_0}|$ is the separation between the diffracted beams and is related to the periodicity of the grating as $|\mathbf{x_0}| = \frac{\lambda f}{a}$ and $\Phi(\mathbf{k})$ is the optical phase of the target beam profile and is given by,

$$\Phi(\mathbf{k}) = \mathrm{Arg}(F(\mathbf{k})).$$

where $\mathrm{Arg}(F(\mathbf{k}))$ returns the arguement of the complex function $F(\mathbf{k})$.

In order to make sure that $G(\mathbf{k})$ is always positive for it to have a physical meaning for the DMD (since the DMD cannot invert the sign of the field) one is added to the cosine function in the Equation 2.9. The inverse Fourier transform of this grating function is given as follows,

$$\begin{aligned} g(\mathbf{x}) &= \mathcal{F}^{-1}[G(\mathbf{k})], \\ &= \frac{1}{4}f(\mathbf{x} + \mathbf{x_0}) + \frac{1}{4}f^*(-\mathbf{x} + \mathbf{x_0}) + \frac{1}{2}\mathcal{F}^{-1}[|F(\mathbf{k})|]. \end{aligned} \tag{2.10}$$

Thus, the inverse Fourier transform gives us three terms known as the first ($m = +1$), negative-first ($m = -1$), and the zeroth order ($m = 0$), where the first and negative-first orders are complex conjugates of each other. The first order corresponds to the target beam profile with a shifted origin ($\mathbf{x_0}$). This idea can be extended for a more ideal case where we take into consideration the electric field profile of the input beam and map the system aberration in the grating equation. The modified grating equation is given as

$$G'(\mathbf{k}) = \eta \left| \frac{F(\mathbf{k})}{E_{\mathrm{in}}(\mathbf{k})} \right| \frac{1}{2}(\cos(\mathbf{x_0} \cdot \mathbf{k} + \Phi(\mathbf{k}) - \Phi_{\mathrm{in}}(\mathbf{k})) + 1), \tag{2.11}$$

where $E_{\mathrm{in}}(\mathbf{k})$ is the electric field profile of the input beam on the surface of the DMD, $\Phi_{\mathrm{in}}(\mathbf{k})$ is the phase profile of the input beam on the DMD, which includes the aberration map and is given by,

$$\Phi_{\mathrm{in}}(\mathbf{k}) = \mathrm{Arg}(E_{\mathrm{in}}(\mathbf{k})),$$

and η is a normalization factor to ensure $0 \leq G'(\mathbf{k}) \leq 1$ and is given by,

$$\eta = \max(\left|\frac{E_{\text{in}}(\mathbf{k})}{F(\mathbf{k})}\right|).$$

Similar to Equation 2.10, we can obtain the three diffraction orders at the IP,

$$\begin{aligned} E_{\text{IP}}(\mathbf{x}) &= \mathcal{F}^{-1}[(E_{\text{in}}(\mathbf{k})G(\mathbf{k}))], \\ &= \eta(\frac{1}{4}f(\mathbf{x}+\mathbf{x_0}) \\ &+ \frac{1}{4}f^*(-\mathbf{x}+\mathbf{x_0}) * \mathcal{F}^{-1}[e^{i(2\Phi_{\text{in}}(\mathbf{k}))}] \\ &+ \frac{1}{2}\mathcal{F}^{-1}|F(\mathbf{k})|e^{i\Phi_{\text{in}}(\mathbf{k})}). \end{aligned} \tag{2.12}$$

The terms are ordered in the same convention as in the Equation 2.10. We can see that the first-order term is free from the input aberration phase, whereas the negative first-order term suffers from twice the aberration. There is also some residual aberration in the zeroth-order beam. Changing the sign of the phase from $\Phi(\mathbf{k}) - \Phi_{\text{in}}(\mathbf{k})$ to $-(\Phi_{\mathbf{k}} - \Phi_{\text{in}}(\mathbf{k}))$ will make the negative-first order beam aberration free instead of the first order beam.

The binary amplitude control of the DMD requires the continuous grating function, $G(\mathbf{k})$, to be binarized. Due to the nonlinear nature of binarization, binarizing a continuous grayscale hologram leads to binarization errors, which result in optical artifacts around the target profile in the IP. To minimize such binarization errors, different methods have been suggested [49, 50, 51, 52].

IFTA

The Iterative Fourier Transform Algorithm (IFTA) has proven to be an efficient algorithm and has been a state-of-the-art in reducing intensity crosstalk (I_X) in the individual addressing beam in the existing results discussed in Section 2.4. IFTA uses a binarized grating function approximated to the grayscale grating, $G_{\text{b}}(\mathbf{k}) \approx G(\mathbf{k})$, such that the binarization artifacts are reduced to a minimum within a signal window $\mathcal{D}$. The binarized grating function is given as,

$$G_{\text{b}}^{(i)}(\mathbf{k}) = U_t[G^{(i)}(\mathbf{k})] = \begin{cases} 0 & \text{if } \text{Re}[G^{(i)}(\mathbf{k})] < t, \\ 1 & \text{if } \text{Re}[G^{(i)}(\mathbf{k})] > (1-t), \\ \text{Re}[G^{(i)}(\mathbf{k})] & \text{otherwise.} \end{cases} \tag{2.13}$$

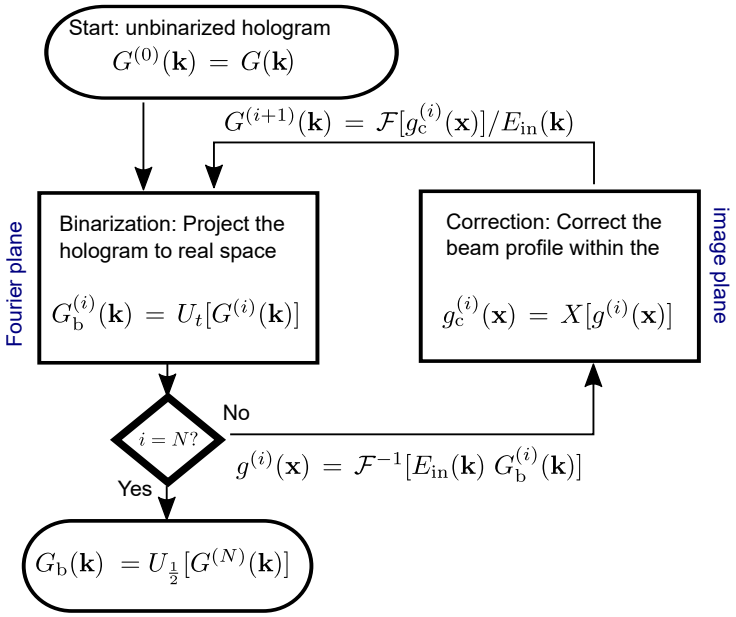


Figure 2.7: Flowchart for IFTA [48].

This grating function follows a dynamic-thresholding approach as mentioned in Wyrowski (1980) [53]. U_t is a binarization operator where t is the dynamic threshold calculated for an iteration number i as follows,

$$t = \frac{i}{2N}, \tag{2.14}$$

where N is the total number of iterations.

A beam profile correction is applied for each iteration within the specified window D to remove binarization errors with the help of an operator X, given by,

$$g_c^{(i)}(\mathbf{x}) = X[g^{(i)}(\mathbf{x})] = \begin{cases} g(\mathbf{x}) & \text{if } \mathbf{x} \in \mathcal{D}, \\ g^{(i)}(\mathbf{x}) & \text{otherwise}, \end{cases} \tag{2.15}$$

where $g(\mathbf{x})$ is the beam profile obtained from the grayscale grating given as $g(\mathbf{x}) = \mathcal{F}^{-1}[E_{in}(\mathbf{k})G(\mathbf{k})]$. The flowchart diagram for IFTA is given in Figure 2.7.

2.6 Aberration Compensation

One key advantage of using Fourier holography with a DMD is the capability to do in-situ aberration compensation. The aberration map incident on the DMD (as defined in Equation 2.11) can be characterized with the help of the DMD. This input aberration is eventually compensated in the first-order diffracted beam as the input aberration term disappears, thus resulting in an aberration-free intensity profile at the image plane.

The DMD's small pixel size, typically ranging between 7.6 μm and 10 μm for different models, offers significantly higher spatial resolution compared to other methods like using Shack-Hartmann wavefront sensors. These sensors rely on micro-lens arrays with a diameter exceeding 150 μm, which limits their resolution. Furthermore, the beam size at the image plane is usually quite small (ranging from a few microns to about 30 μm), making Shack-Hartmann sensors a non-ideal choice.

I follow the approach mentioned in Dr. Chung You-Shih's Master's Thesis (2019) [48] for extracting the aberration phase profile. It follows a method demonstrated in Zupancic (2013) [52] where two patches are turned on on the DMD at the FP and the respective interference pattern is observed at the IP. This interference pattern contains information about the path difference between the patches as well as the spatial phase difference, which can be extracted in the post-processing. To understand how I characterize the aberration map, I will follow along the derivation given in [48].

Let us assume two small patches are turned on the DMD surface, separated by a distance d. This results in nearly plane waves at the image plane as a result of the optical Fourier transform of small patches. Let $E_1(\mathbf{x})$ and $E_2(\mathbf{x})$ represent the electric field corresponding to each patch at the IP with optical phases ϕ_1 and ϕ_2 respectively.

$$E_1(\mathbf{x}) = A_1 e^{i(\mathbf{k_1}\cdot\mathbf{x}+\phi_1)}, \tag{2.16}$$

$$E_2(\mathbf{x}) = A_2 e^{i(\mathbf{k_2}\cdot\mathbf{x}+\phi_2)}. \tag{2.17}$$

These two electric fields interfere at the IP and thus give a resultant interference pattern (an example has been shown in Figure 2.8) with intensity given by:

$$I_{\text{tot}}(\mathbf{x}) = |E_1(\mathbf{x}) + E_2(\mathbf{x})|^2, \tag{2.18}$$

$$= |A_1|^2 + |A_2|^2 + 2A_1A_2 \cdot \cos((\mathbf{k_1} - \mathbf{k_2})\cdot\mathbf{x} + \phi_1 - \phi_2). \tag{2.19}$$

We can extract the spatial phase information from the Equation 2.18. One key thing to understand here is that the aberration map obtained using this method is a relative

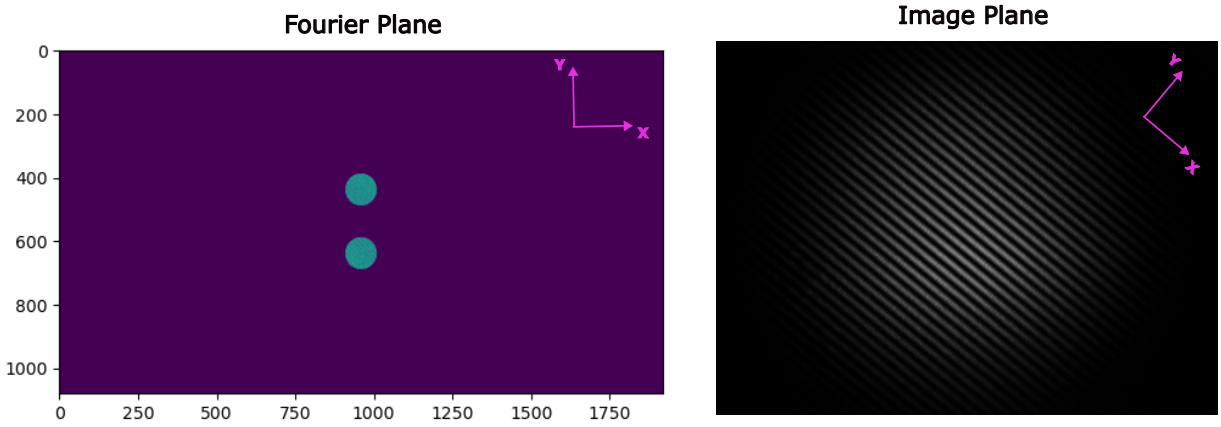


Figure 2.8: Left shows a virtual image of the DMD in the FP, where two patches (not to scale) have been turned on. Right shows an image of the interference pattern as seen on a camera. The axes on the camera (IP) are tilted by a 45° angle since the DMD is mounted at 45° on the optics table to ensure the propagation direction of the reflected beam is parallel to the optics table (Figure 3.3).

aberration map. We first create a grid of patch centers based on the resolution we want, which decides the patch size and separation. The reference patch, which is the center-most patch, is turned on at all times, and the scanning patch is scanned across the grid one by one. For each position of the scanning patch, the resultant fringe pattern is captured on the camera. In the post-processing, a 1D profile $f(\mathbf{x})$ is obtained by summing the image along the axis perpendicular to the direction of the two patches, i.e., perpendicular to $(\mathbf{k_1} - \mathbf{k_2})$. Then the spatial phase difference, $\psi = \phi_1 - \phi_2$ is extracted by taking a correlation [1] between $f(\mathbf{x})$ and a test signal $e^{i\mathbf{k}(\mathbf{x}-\mathbf{x_0})}$,

$$C = \mathrm{corr}(e^{i\mathbf{k}(\mathbf{x}-\mathbf{x_0})}, f(\mathbf{x})), \tag{2.20}$$

where $\mathbf{k}$ is the spatial frequency of the interference fringe, which is given by,

$$\mathbf{k} = |\mathbf{k_1} - \mathbf{k_2}| = \frac{2\pi}{\lambda f}\Delta, \tag{2.21}$$

where Δ is the separation of two patches.

Thus, a 2D phase profile can be constructed by scanning the patch along a 2D grid and obtaining the spatial phase information for each position of the scanning patch. This

[1] https://numpy.org/doc/stable/reference/generated/numpy.correlate.html

obtained phase map is unwrapped to make it continuous and used as the input aberration map as mentioned in Equation 2.11. The aberration map can be further analyzed by fitting it to a series of Zernike polynomials. A residual phase map can be obtained by repeating the phase map extraction process but passing a negated input aberration map to the carrier grating inside each patch. A significant improvement of about 50 times can be seen in the residual phase map after aberration compensation.

2.6.1 Summary and Outlook

In summary, this chapter outlined the research problem, with a brief introduction to MCMR requirements, and described the approach adopted by our group, i.e., careful engineering of a low-crosstalk individual addressing beam to enable in-situ MCMR. I provided an understanding of the physics involved in the state detection and reset processes in $^{171}Yb^{+}$ and gave a theoretical overview of how an amplitude grating is employed with the DMD, which enables us to do both phase and amplitude modulation of the individual addressing beam. I also discussed the results obtained in the current state-of-the-art individual addressing system, which relies on using IFTA for hologram generation and in-situ aberration compensation and has been able to achieve an intensity crosstalk below 10^{-4} for the entire ion chain (50 ions).

I identified how the existing method can be further optimized in terms of the absolute value of intensity crosstalk at the nearest neighbour, which is more susceptible to AQM due to its proximity to the addressing beam and has the potential to be reduced further below the fundamental limit set by inter-ion scattering given by 10^{-5}. I suggested a novel method of using a secondary grating described in Chapter 3, to further minimize the intensity crosstalk at the nearest neighbor location. Using this method, an absolute crosstalk suppression of up to 6 dB can be seen.

Another suggested improvement was introduced in terms of mitigating long-range crosstalk errors arising from the asymptotic limit reached by the intensity profile of the addressing beam generated using the existing technique, which saturates at sub 10^{-4}. This takes a hit on the net measurement probability due to a constant propagation of errors across the ion chain (> 30 ions). To mitigate this, Chapter 4 suggests using the DMD in a double pass configuration where the DMD acts as an intermediate image plane pupil in the second pass. This method shows promising results by reducing the intensity crosstalk to sub 10^{-6} beyond the third nearest neighbor.

Chapter 3

A Secondary Grating Method

Author's Contributions: The idea of using a secondary beam to mitigate crosstalk at the nearest neighbor was developed in discussions with Prof. Rajibul Islam. The experimental setup design and the method of hologram generation have been adopted by the author from previous research done by Dr. Chung-You (Gilbert) Shih. Setting up the experiment, numerical simulations, execution, and development of protocols for data extraction and analysis were performed by the author.

3.1 Overview

The ion-to-ion separation in the Bloodstone processor is $a = 4$ μm, and the addressing beam has a waist of $w = \frac{a}{4} = 1$ μm. The size of the beam is chosen to ensure a good overlap between the addressing beam and the ion's wave function. The proximity of the nearest-neighbor ions makes them more susceptible to AQM as compared to the ions further away from the center of the addressing beam location.

Using IFTA, the intensity crosstalk has been reduced to below 10^{-4} for the entire chain of ions in Ref. [26]. However, it can be seen in Ref. [44], that the preservation fidelity for measurement (for 11 μs detection time) is $F_{1|2} \geq 99.5\%$ for $d \geq 4w$ and $F_{1|2} \geq 99.9\%$ for $d \geq 20w$, thus suggesting that the average preservation fidelity of asset qubit for mid-circuit measurement of process qubit is limited by the preservation fidelity of the nearest neighbors to the process qubit (See Section 2.4). These preservation fidelity values were obtained assuming a fast detection time of 11 μs, which requires advanced state measurement protocol with high-fidelity detection. Improving the preservation fidelity at

the nearest neighbor will not only improve the average preservation fidelity but will also relax constraints on high-efficiency detection systems and state measurement protocols, which require complicated engineering [46] and will allow longer detection times. Hence, to address the low preservation fidelity of nearest neighbors, this chapter introduces a strategy known as the secondary grating method.

This method relies on using the DMD to generate a secondary beam on top of the primary addressing beam coinciding with the location of the neighboring ion where we want to suppress the intensity crosstalk, I_X. The phase and amplitude control (See Equation 2.11) over the grating that creates this secondary beam allows us to find a suitable value for the parameters to create a local destructive interference. Using this method, I have been able to reduce the intensity crosstalk, I_X, by ≈ 6 dB at $x = 4w$, i.e., the nearest neighbor location.

The results presented in this chapter are up to an intermediate image plane measured with a camera, and can be subsequently relayed to the ion plane through appropriate de-magnification.

3.1.1 Chapter Outline

The chapter outline is given as follows:

- In Section 3.1, I provide a brief overview of the research problem we are trying to address and introduce the secondary grating method.
- In Section 3.2, I discuss the working principle of the secondary grating method and study the dependence of the secondary grating parameters on the image plane intensity.
- In Section 3.3, I describe the experimental setup for the method and talk about the DMD used in the setup along with the relevant lens parameters.
- In Section 3.4, I present the main results obtained using the method along with some error analysis to characterize the noise in the intensity profile of the beam. The data is presented in two different scales, linear and High Dynamic Range (HDR).
- In Section 3.5, I summarize the chapter by reiterating the key results obtained in terms of reduced I_X at the nearest neighbor and its implications in reducing P_{AQM}.

3.2 Theoretical Background

As discussed in Chapter 2, an amplitude grating created using IFTA is used to generate the hologram displayed on the DMD, which produces three orders of diffracted beams at the image plane. Out of which we can use either the first or the negative-first orders, based on the sign of the input aberration map used in the grating function (Equation 2.11), to obtain an aberration-free addressing beam for performing individual measurements and reset on ions. Let us refer to the addressing beam that probes the process qubit as the primary addressing beam, and the corresponding grating as the primary grating. Since we block the undesired orders at the intermediate image plane, when I refer to the image plane beam, I will be referring to the first or negative-first order beam, based on the convention chosen. Let us assume $E_{\mathrm{p}}(x)$ is the electric field of the target beam profile (primary beam) and $F_{\mathrm{p}}(x) = \mathcal{F}(E_{\mathrm{p}}(x))$ be the Fourier transform of $E_{\mathrm{p}}(x)$. For simplicity, the following derivation is presented in one dimension, along the direction of the ion chain, which is the primary axis of interest. For a target Gaussian beam profile centered at x_0 with waist w, $E_{\mathrm{p}}(x)$[1] is given as,

$$E_{\mathrm{p}}(x) = A_1 e^{-\frac{(x-x_0)^2}{w^2}} e^{i\Phi(x)}, \tag{3.1}$$

where A_1 is a constant amplitude and $\Phi(x)$ is the spatial phase profile.

Let us assume the inter-ion separation is a; therefore, for a process qubit at $x = x_0$, the position of the next neighbor is given by $x = x_0 \pm a$. For an asset qubit at $x = x_0 + a$, the electric field of the primary beam is given by,

$$\begin{aligned} E_{\mathrm{p}}(x = x_0 + a) &= A_1 e^{-\frac{(a)^2}{w^2}} e^{i\Phi(x_0+a)}, \\ &= \tilde{A}_1 e^{i\phi_1}, \end{aligned} \tag{3.2}$$

where $\tilde{A}_1 = A_1 e^{-\frac{(a)^2}{w^2}}$ and $\Phi(x_0 + a) = \phi_1$.

We use a small portion of the DMD to create a secondary beam at the location of the neighboring ion ($x = x_0 + a$) as shown in Figure 3.1. Thus, a rectangular window with dimensions ($l \times m$) is taken on the Fourier plane, and a secondary grating is added on top of the primary grating where l is along the axis that corresponds to the ion-axis in the image plane. The secondary grating at the Fourier plane (in 1D) is given by,

[1]Here, the electric field is given as a complex function, but only the real part of the expression corresponds to the physical electric field.

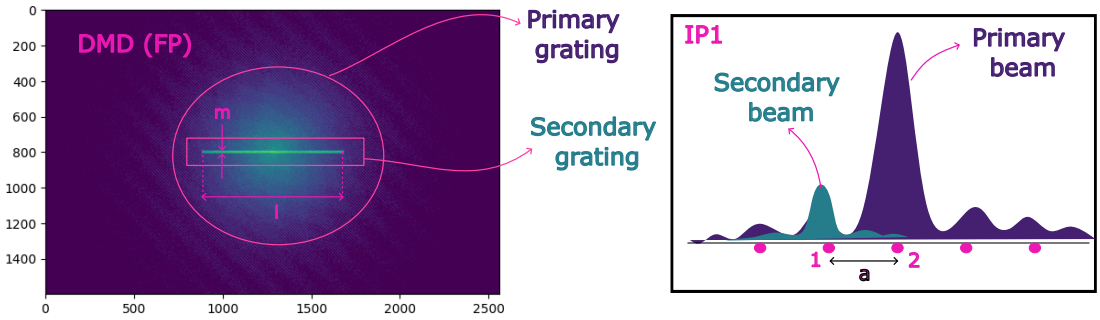


Figure 3.1: Left shows a picture of the grating state of the DMD. There is a larger grating in the background which corresponds to the primary grating. Lying on top of the primary grating is a secondary grating within a rectangular window ($l \times m$). Right shows a picture of Image Plane 1 (IP1) where the primary beam falls on the mapped position of Ion 2 (process qubit) in the IP1. The secondary beam falls on the mapped position of Ion 1 (asset qubit). The ion-to-ion separation is given by a. We can optimize the phase and amplitude of the secondary beam by changing the phase (ϕ_2) and the amplitude (A_2') parameters in the secondary grating to create a local destructive interference.

$$F_{\mathrm{s}}(x) = \frac{\eta}{E_{in}(x)} \times A_2' \times \mathrm{rect}(\frac{\mathrm{x}}{\mathrm{l}}) \times \frac{1}{2} \times (\cos(2\pi \frac{x_a \cdot x}{\lambda f} + \Phi(x) - \Phi_{in}(x)) + 1), \tag{3.3}$$

where x_a corresponds to the periodicity of the grating for position $x = x_0 + a$ and $\Phi(x)$ is set to a constant phase ϕ_2 and $\mathrm{rect}(\frac{x}{l})$ is given by,

$$\mathrm{rect}(\frac{x}{l}) = \begin{cases} 0 & \text{for } x > l/2 \text{ or } x < -l/2, \\ 1 & \text{for } -l/2 \leq x \leq l/2. \end{cases}$$

Therefore, using Equation 2.12, the electric field of the secondary beam (first-order) at the image plane is given by,

$$E_{\mathrm{s}}(x) = A_2 l \ \mathrm{sinc}(kl) e^{i\phi_2}\big|_{k=\frac{2\pi}{\lambda f}(x-(x_0+a))}, \tag{3.4}$$

$$= A_2 l \mathrm{sinc}(\frac{2\pi}{\lambda f}(x - (x_0 + a))l) e^{i\phi_2}. \tag{3.5}$$

Therefore, for $x = x_0 + a$, we have,

$$E_{\mathrm{s}}(x = x_0 + a) = A_2 l e^{i\phi_2}, \\ = \tilde{A}_2 e^{i\phi_2}. \tag{3.6}$$

Since the sum of two functions in the Fourier plane corresponds to the sum of the individual Fourier transforms of the functions in the image plane, we have the resultant electric field at the image plane (IP),

$$\begin{aligned} E_{\mathrm{IP}}(x) &= E_{\mathrm{p}}(x) + E_{\mathrm{s}}(x), \\ &= A_1 e^{-\frac{(x-x_0)^2}{w^2}} e^{i\Phi(x)} + A_2 l \mathrm{sinc}(\frac{2\pi}{\lambda f}(x-(x_0+a))l) e^{i\phi_2}. \end{aligned} \tag{3.7}$$

Therefore, at $x = x_0 + a$,

$$E_{\mathrm{IP}}(x = x_0 + a) = \tilde{A}_1 e^{i\phi_1} + \tilde{A}_2 e^{i\phi_2}. \tag{3.8}$$

The resultant intensity at the asset qubit position is,

$$I_{x_0+a} = |E_{\mathrm{IP}}(x = x_0 + a)|^2 = \tilde{A_1}^2 + \tilde{A_2}^2 + 2\tilde{A}_1\tilde{A}_2 \cos(\phi_1 - \phi_2), \tag{3.9}$$

$$\text{and } I_{x_0+a,\ \mathrm{min}} = (\tilde{A}_1 - \tilde{A}_2)^2. \tag{3.10}$$

Thus, we can optimize the phase (ϕ_2) and amplitude (A_2') of the secondary beam such that $\phi_1 - \phi_2 = 2n+1 \cdot \pi$ (where n is an integer) and $\tilde{A_1} \approx \tilde{A_2}$, which will create a local destructive interference at the neighboring ion location, thus minimizing the resultant intensity. This method can be extended to suppress the resultant intensity at any location in the ion chain.

3.3 Experimental Setup

The previously described results using Fourier holography and IFTA were obtained in the Amethyst Processor, which is based on a four-rod Paul trap. This section describes an independent experimental setup used to verify the secondary grating method. Some of the parameters, such as the DMD, the objective numerical aperture (NA), ion-to-ion spacing, and de-magnification, are different in the Bloodstone Processor. This section also provides details on the changed parameters and the relevant calculations.

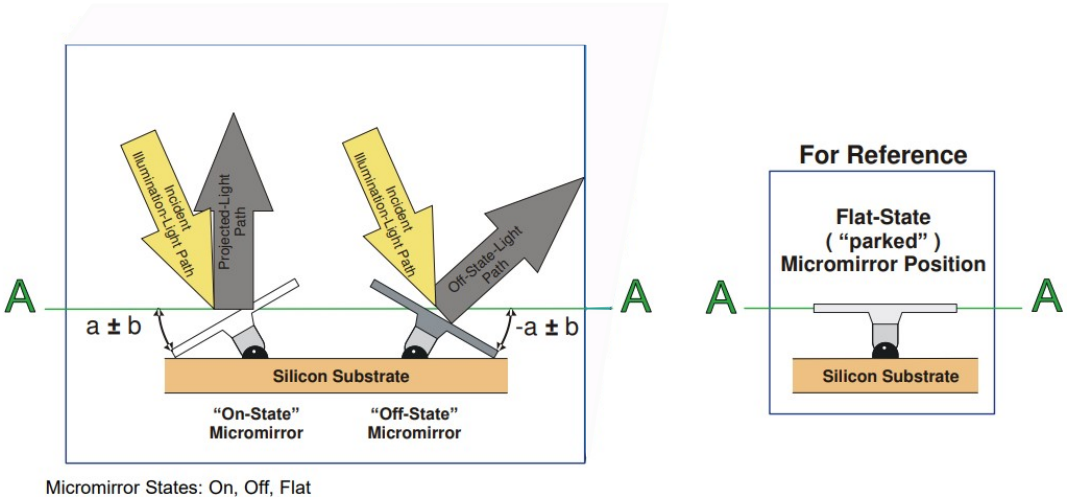


Figure 3.2: Figure showing the ON ($+12°$) and OFF ($-12°$) state of the DMD micro mirrors with respect to the flat reference position. Figure has been adapted and edited from DLP9000XUV datasheet [54].

3.3.1 Bloodstone Parameters

DLP9000XUV

The adaptive optics used to generate the reprogrammable hologram is a DMD from Texas Instruments, DLP9000XUV. An FGPA controller from ViALUX GmbH is used as the controller. This DMD consists of a 2D array of > 4 million micro mirrors, thus giving a high resolution of 2560×1600 pixels. The micro mirror pitch is 7.6 μm and each micro mirror can alternate between two tilt angles of $\pm 12°$ (Figure 3.2). The DMD is based on a micro-electrical-mechanical system (MEMS) technology and has a fast refresh rate of $\approx$ 15 kHz. The direction of the mirror axis lies along the diagonal of the DMD; hence, to keep the optical axis along the optics table, the DMD is mounted at a 45° angle with respect to the optics table (Figure 3.3). This DMD offers a higher resolution and a faster switching time, which might help in getting an aberration map with finer resolution and also decrease process time. This DMD is also designed for UV wavelengths (355 nm to 420 nm) and has a micro mirror reflectivity of about 88%. PySLM2 [55] has been used to generate the programmable hologram, which is passed to the DMD.

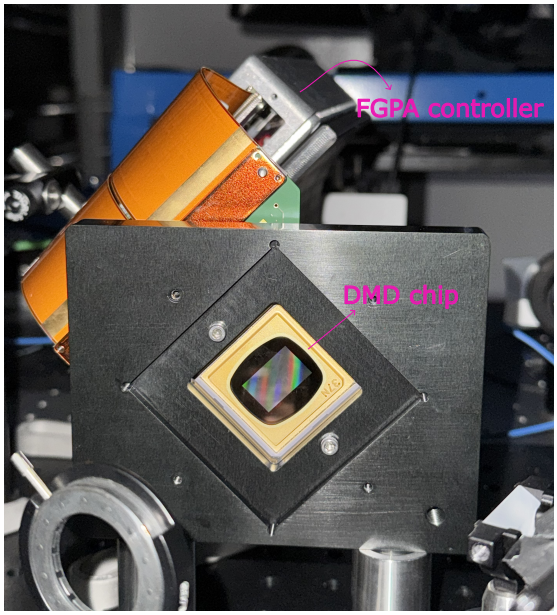


Figure 3.3: DMD (DLP9000XUV) mounted at a 45° angle to ensure that the reflected light from the DMD is parallel to the optics table because the axis of the micro mirrors lies along the diagonal direction with respect to the DMD.

Lens Parameters

To understand how we plan to relay our addressing beam to the ions, we can refer to the Figure 3.4. A suitable collimating lens is used to collimate the beam coming out of the fiber, creating a beam with a waist of 5 mm that matches the aperture of the DMD. The collimated beam, after reflecting from the DMD, passes through a lens (Fourier lens) and focuses down to an intermediate image plane, Image Plane 1 (IP1). The beam is further relayed onto the Ion plane using another lens, which acts as the beam expander, and focused down by the objective.

A 0.3 NA objective will be used to focus down the individual addressing beam onto the Ion plane in the Bloodstone processor. To use the full aperture of the objective, there is a three times magnification of the collimated beam from the Fourier plane to the objective entrance, which would result in $f_3 \approx 3 \times f_2$. To account for compactness, we would like to have a shorter focal length f_2. Since f_2 is the focal length of the Fourier lens used to generate the interference fringe pattern to extract the aberration map, we need to make sure that f_2 is suitably above the Nyquist limit to obtain a good fringe contrast on the camera at IP1. Based on this, a 150 mm lens is chosen as the Fourier lens with Nyquist

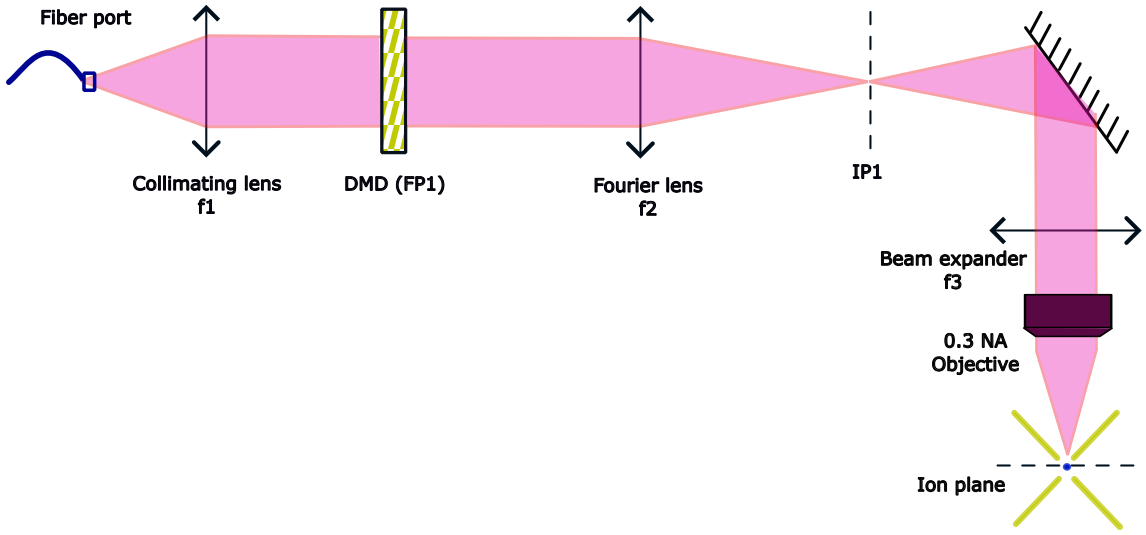


Figure 3.4: A qualitative schematic of the whole relay optics for the individual addressing beam. The DMD is shown as a transmissive element for simplicity.

frequency equivalent to 3 pixels for a pixel size of 1.85 μm. This sets the demagnification from IP1 to Ion plane to 9 times.

To verify the secondary grating method, all characterizations have been done until the IP1, and the data is in the form of an intensity profile measured with a camera at the IP1.

3.3.2 Optical Schematic

The optical setup (Figure 3.5) consists of a collimating lens with a focal length of 75 mm, which collimates the light (369 nm) coming out of a Polarization Maintaining (PM) fiber. The collimated light falls on the DMD, which is displaying both the primary and the secondary grating. The engineered wavefront reflected from the surface of the DMD gets focused by a Fourier lens of focal length 150 mm. A CMOS camera (FLIR BFS-PGE-120S4M-CS) is placed at the corresponding image plane (IP1). The power efficiency of the negative first order can be improved with an additional correction operator applied during the IFTA binarization process, as shown in Ref. [56]; hence, the negative first order is used for this experiment, and the other orders are kept blocked.

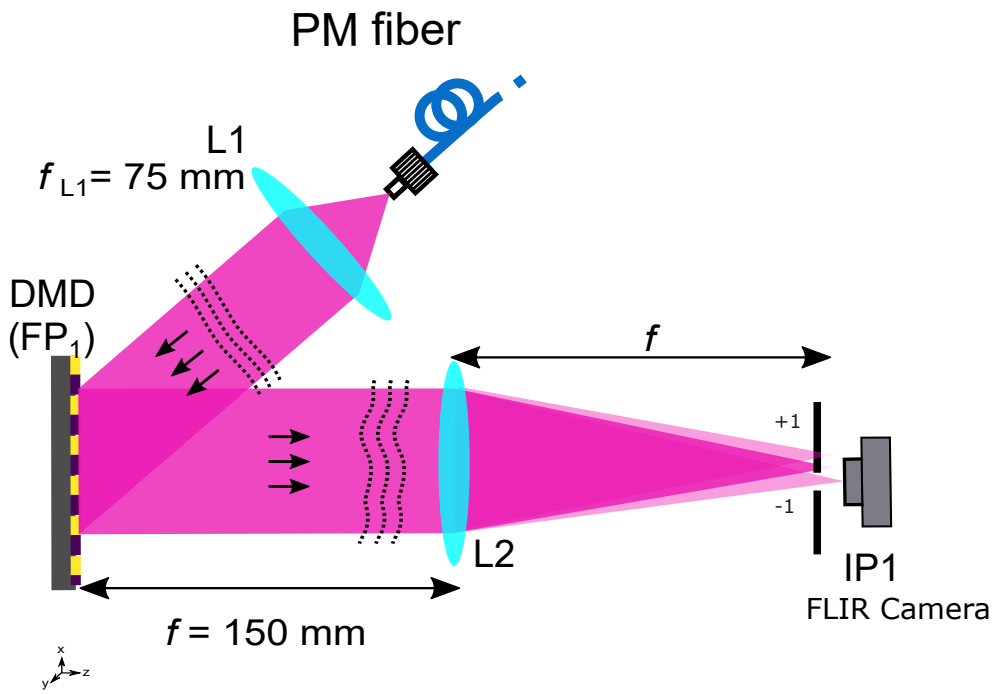


Figure 3.5: Optical schematic for the secondary grating method.

3.3.3 Methodology

The desired beam waist of the addressing beam at the Ion plane is 1 μm, therefore, considering 9 times de-magnification from IP1 to the Ion plane, the waist of the primary beam at IP1 is set to $w_{\text{IP1}} = 9$ μm. This method is used to create an intensity minimum at the ion location corresponding to $4w_{\text{IP1}}$. The methodology used is given as follows:

- The primary grating is passed to the DMD, and a HDR image of the primary beam is taken on the camera. The intensity of the beam at the location corresponding to $4w_{\text{IP1}}$ is extracted.
- A region of interest (ROI) is removed from the base grating to create room for the secondary grating. The breadth of the ROI is fixed to three pixels, and the length of the ROI is chosen arbitrarily based on the length of the secondary grating window needed.

- The size of the secondary grating window is chosen such that there is enough dynamic range to vary the amplitude of the secondary beam by changing the amplitude of the grating function (A_2').
- For a fixed amplitude, the phase (ϕ_2) (Equation 3.9) of the secondary beam is scanned, varying it from 0 to 4π. The intensity of the beam at $4w_{\mathrm{IP1}}$ is extracted and plotted against different values of phase, ϕ_2. The value of phase ($\phi_{2,\mathrm{min}}$) corresponding to the location of minimum intensity is extracted from the plot.
- Once the optimum value of the phase ($\phi_{2,\mathrm{min}}$) is obtained, the amplitude (A_2') of the secondary beam is scanned keeping the phase fixed at $\phi_2 = \phi_{2,\mathrm{min}}$ to further optimize the minimum intensity at $4w_{\mathrm{IP1}}$.

3.4 Results: Measurement of Intensity Crosstalk

3.4.1 Focal length calibration

The effective focal length of the system is calibrated by creating a Gaussian beam with waist $w = 9$ μm at different locations at the IP1. This is achieved by adjusting the value of the periodicity of the primary grating function. Thus, a $w = 9$ μm beam is generated at IP1, and the position of the beam is moved along the direction of the ion chain. The actual position of the beam is verified by the measurements taken with the camera. From a linear fit of the data, the effective focal length is extracted to be 161 mm.

3.4.2 Camera calibration

A CMOS camera (FLIR BFS-PGE-120S4M-CS) is used for data extraction. The linear response of the camera to a change in intensity is calibrated as shown in Figure 3.7. This is achieved by measuring the pixel value of the brightest pixel on the camera as the power of the beam falling on the camera is increased for a fixed exposure setting (120 μs).

3.4.3 Aberration Data

The input aberration map is characterized using the method described in Section 2.6. The total aberration phase map, $\Phi_{\mathrm{in}}(x)$ is obtained in two steps $[\Phi_0(x) + \Phi_1(x)]$ as in Ref. [26].

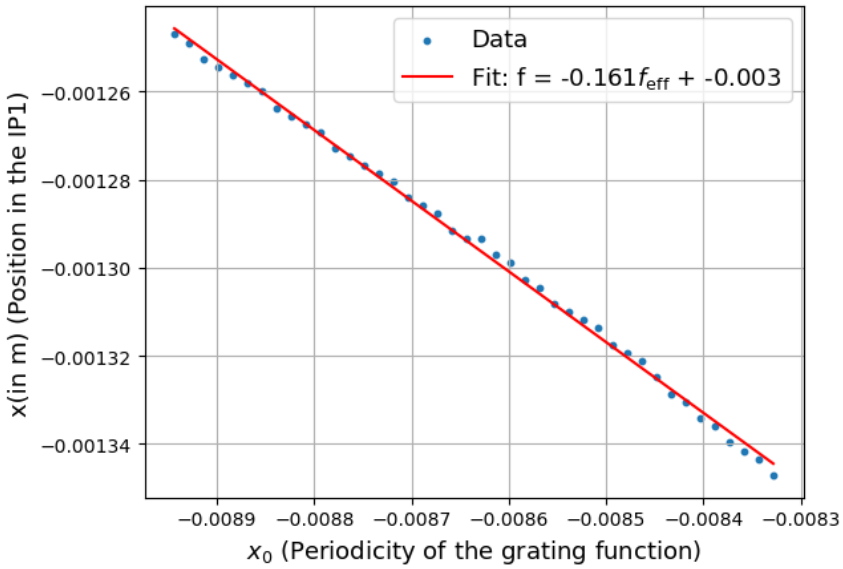


Figure 3.6: Plot between periodicity of grating corresponding to different beam positions along ion chain axis and the beam position extracted from the camera. The curve is fitted to a linear model and the effective focal length obtained is 161 mm.

The majority of the aberration from the input source to the IP1 is characterized using $\Phi_0(x)$. For this, a patch size of 8×8 micro mirror pixels and a grid size of 20 pixels is chosen. A reference patch is turned on in the center ($x = 0$), and another patch is scanned across the grid ($x = \Delta$). For the extraction of $\Phi_0(x)$, I keep all the mirrors on within a patch. I measured $\Phi_0(x)$ to be 9.8λ (19.6π) peak-to-peak and 1.75λ RMS.

I characterize the additional aberrations, i.e., $\Phi_1(x)$, using the phase map $\Phi_0(x)$ as feedback. I use circular patches of diameter 30 pixels and supply an amplitude grating to each patch with an input phase of $\Phi_0(x)$. I measure the additional aberration to be 2.01λ (4π) peak-to-peak and 0.4λ RMS (Figure 3.8). The size of the Fourier plane chosen for characterizing $\Phi_0(x)$ and $\Phi_1(x)$ is 1600 pixels and 1480 pixels, respectively. After compensating for the aberration, the residual aberration could be reduced to 0.15λ (0.3π) peak-to-peak and 0.014λ RMS.

3.4.4 Intensity Crosstalk Data

A primary grating corresponding to a Gaussian beam with a waist 9 μm is created at the IP1 ($x = 0$). This serves as the primary beam. A High Dynamic Range (HDR) image of

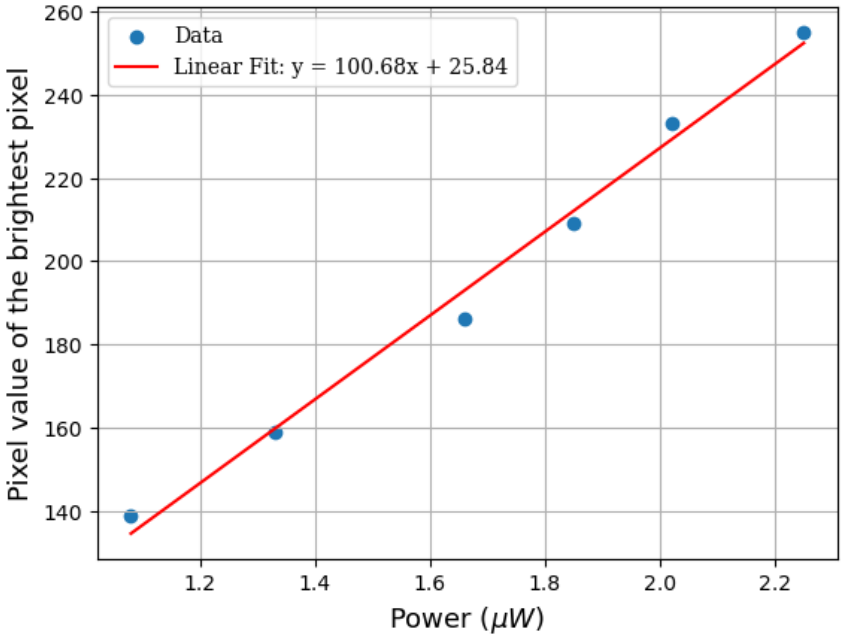


Figure 3.7: Figure showing calibration of the camera (FLIR BFS-PGE-120S4M-CS) used for data extraction. A linear change in the pixel value can be seen with the increase in input power of the beam falling on the camera.

the primary beam is obtained, and the intensity of the beam at the mapped location for the neighboring ion, i.e. $x = 4w_{\text{IP1}}$, is extracted. This intensity, denoted by I_{x_0+a} as given in Equation 3.9, is the intensity crosstalk, I_X. Following the methodology mentioned in Subsection 3.3.3, a suitable rectangular window is removed from the primary grating. This serves as the ROI for the secondary grating. I chose an ROI with a width of 3 pixels and a length of 600 pixels. This will have some implications for the primary beam, but doesn't affect the intensity along the ion axis, which is the primary axis of interest. A secondary grating ($F_s(x)$) with a width of 2 pixels and a length of 460 pixels is added on top of the primary grating on the DMD as shown in Figure 3.1. Thus, two beams are created at the image plane, the primary beam and a secondary beam at the neighboring ion location ($x = 4w_{\text{IP1}}$). The amplitude and the output phase of the secondary beam can be changed by changing $A_2'(x)$ and $\Phi(x)$ in the secondary grating function (Equation 3.9).

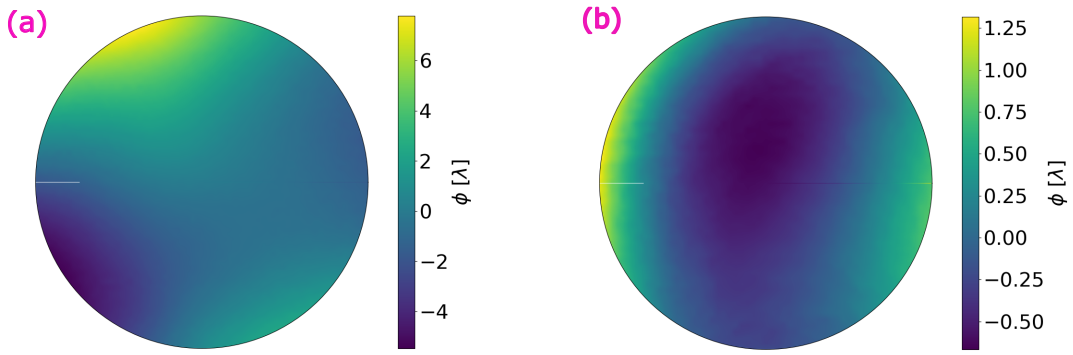


Figure 3.8: Aberration phase map (Radius of the Fourier plane is 700 pixels) (a) $\Phi_0(x)$ is measured to be 9.8λ (19.6π) peak-to-peak and 1.75λ RMS. (b) $\Phi_1(x)$ is measured to be 2.01λ (4π) peak-to-peak and 0.4λ RMS.

Linear Scale Data

The working of the method is first verified by looking at the absolute pixel value obtained from a single camera image for different values of $A_2'(x)$ and ϕ_2. Let us call this the linear scale.

First, I determine the optimal phase of the secondary beam for which there is a local destructive interference at $x = 4w_{\text{IP1}}$, and hence a reduction in the absolute intensity crosstalk value ($I_X = I_{x_0+a}$). The input power is set to 25 μW and exposure is set to 1.2 s. I set the amplitude of the secondary grating at $A_2' = 0.7$, which implies that the mirrors are turned on the grating with a 70% sampling probability. The phase of the secondary beam is scanned in the range $\phi_2 \in [0, 4\pi]$ and corresponding images are taken on the camera at IP1. The pixel value [0, 255] for each camera image at $x = 4w_{\text{IP1}}$ is plotted against the respective phase of the secondary beam. In Figure 3.9, a cosine dependence can be seen in the pixel value measured at $x = 4w_{\text{IP1}}$ with the phase ϕ_2. A dip in I_X at $\phi_2 = \pi$ from 79 to 50, i.e. 36% reduction can be seen, where pixel value 79 corresponds to the I_X from the primary beam alone. $I_{X,\text{min}}$ is further optimized by keeping the phase of the secondary beam fixed $\phi_2 = \pi$ and scanning the amplitude of the beam A_2' from 0.1 to 1. A further reduction of I_X at $A_2' = 0.44$ can be seen. The pixel value at $x = 4w_{\text{IP1}}$ gets suppressed to 43 from 79 using this method for the optimal value of $\phi_2 = \pi$ and $A_2' = 0.44$. Thus, a net suppression of 38.6% can be seen in I_X at the nearest neighboring ion position at the IP1.

HDR Data

The linear scale does not give complete information about the intensity crosstalk, I_X, as the primary beam region is saturated. This limits the dynamic range, and the measurement is also more susceptible to input power fluctuations. Hence, I also take HDR images for different values of ϕ_2 and A_2' of the secondary beam. The input power to the DMD is fixed at 15 μW, and images are taken at different exposure values ranging from 120 μs to 12 s for each data point and stitched together. The normalized intensity crosstalk (I_X) is measured at $x = 4w_{\text{IP1}}$ for different values of ϕ_2 and A_2'.

A similar trend can be seen in the phase scan and amplitude scan plots shown in Figure 3.10. I_X corresponding to the primary beam is measured as $10^{-4.3}$. A dip in the intensity can be seen for $\phi_2 = \pi$ in the phase scan curve, where the intensity drops to $10^{-4.75}$, which is ≈ 5 dB suppression in I_X. Further optimization is done to obtain $I_{X,\text{min}}$ by doing an amplitude scan at $\phi_2 = \pi$. A net suppression of ≈ 6 dB can be seen after optimizing for A_2' ($= 0.38$).

3.4.5 2D scan

A 2D scan is also done where the phase (ϕ_2) and amplitude (A_2') of the secondary beam are varied, and single-exposure images are taken on the camera. The I_X in terms of the pixel value is plotted for $x = 4w_{\text{IP1}}$. Regions of minimum intensity can be seen in the amplitude vs phase space with periodicity of 2π (Figure 3.11). Suppression of I_X can be seen from 98 to 45.5 in terms of pixel value, i.e., 53.57%.

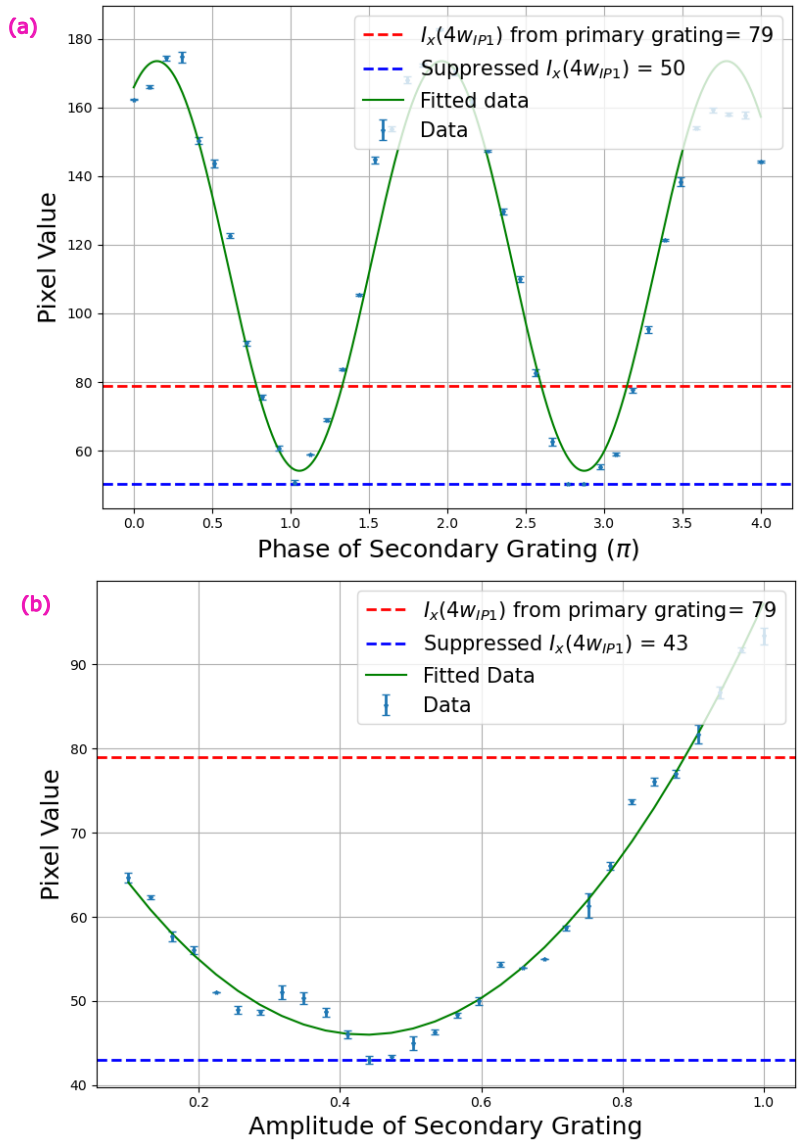


Figure 3.9: **Linear Scale Data**: Pixel value at $x = 4w_{\mathrm{IP1}}$ from the primary beam alone is 79. (a) Phase (ϕ_2) of the secondary beam is scanned keeping the amplitude (A_2') fixed at 0.7 and the pixel value at $x = 4w_{\mathrm{IP1}}$ is plotted. Suppression of I_X can be seen for $\phi_2 = \pi$ where the pixel value dips to 50, i.e. 36% suppression. (b) Amplitude (A_2') of the secondary beam is scanned keeping the phase (ϕ_2) fixed at π and the corresponding pixel value at $x = 4w_{\mathrm{IP1}}$ is plotted. A further suppression in the pixel value to 43, i.e. 38.6% can be seen for $A_2' = 0.44$. The error bars represent the standard error for 3 shots, where each shot represents an image taken on the camera for an exposure value of 1.2 s.

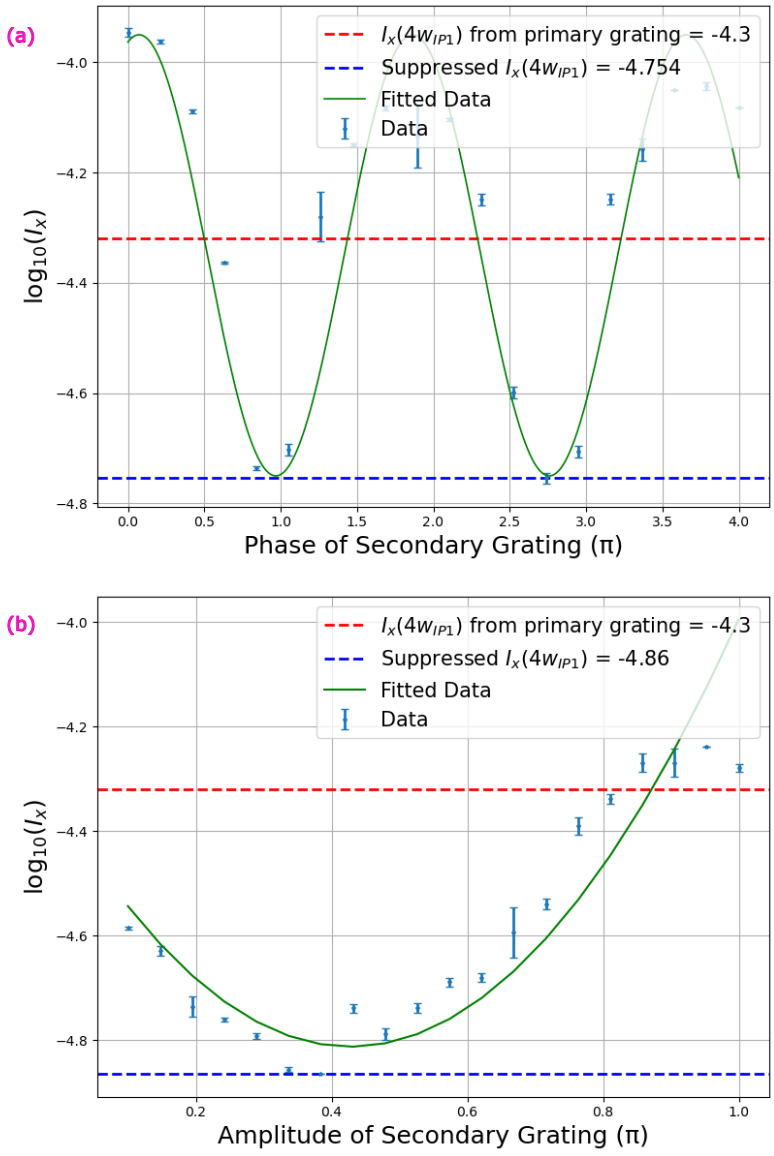


Figure 3.10: **HDR Data**: I_X from primary beam is $10^{-4.3}$. (a) Phase (ϕ_2) of the secondary beam is scanned keeping the amplitude (A_2') fixed at 0.7, and the normalized I_X obtained from the HDR images is plotted. Suppression in I_X by ≈ 5 dB can be seen for $\phi_2 = \pi$. (b) Amplitude (A_2') of the secondary beam is scanned keeping the phase (ϕ_2) fixed at π and the corresponding normalized I_X is plotted. A further suppression of I_X, i.e., ≈ 6 dB, is seen after optimizing A_2' to 0.38. The error bars represent the standard error computed from 3 HDR images computed from taking 3 shots of images at exposure settings ranging from 120 μs to 12 s.

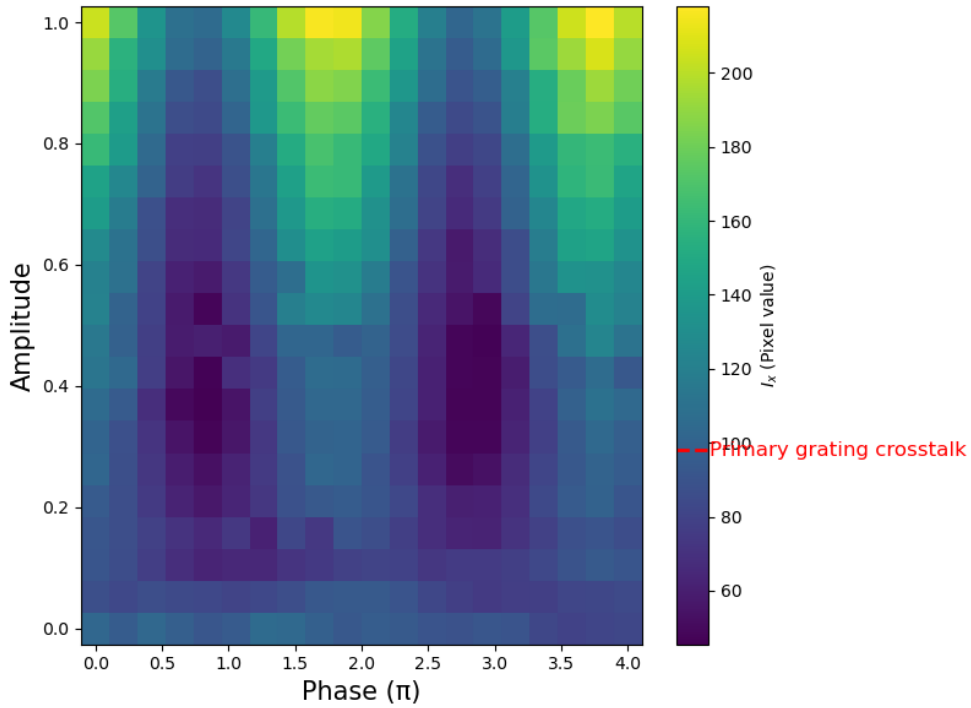


Figure 3.11: A 2D colourmap representing the I_X for different values of phase ($\phi_2 \in [0, 4\pi]$) and amplitude ($A_2' \in [0, 1]$). Periodic pockets of minima can be seen in amplitude and phase space as expected from Equation 3.9. Primary grating crosstalk (marked in red) refers to the I_x (Pixel value at $4w_{IP1}$) when only the primary grating is displayed on the DMD.

3.4.6 Error Analysis

Beam center fluctuation

The beam center location of the primary beam is susceptible to fluctuations arising from either the sensor of the camera or thermal fluctuations around the beam. Here, the location of the beam center is given by the brightest pixel on the camera. It is important to calibrate the beam center location because the position of the asset qubit is referenced to this point. Hence, for each data point in the linear scan, a low-exposure image is also taken along with the high-exposure images to pinpoint the center of the primary beam. Figure 3.13 shows the fluctuation in the location of the beam as seen during the 2D scan given in Figure 3.11

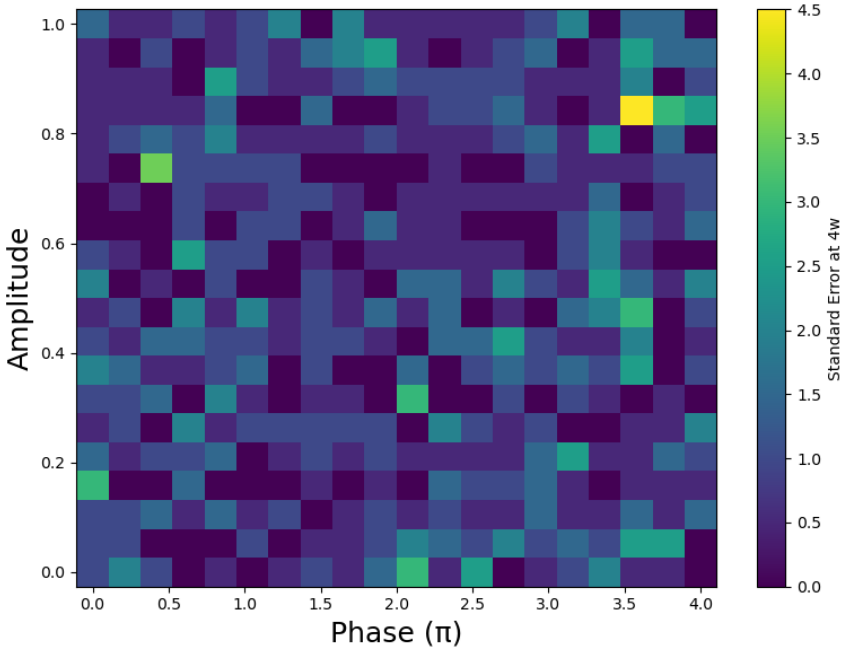


Figure 3.12: A standard error map for the for the 2D scan mentioned in Figure 3.11 with mean standard error of 0.82.

Intensity Fluctuation

Since the suppression in I_X in the HDR scale is comparable to the intensity fluctuations/noise level, it is important to characterize the fluctuations or noise in the intensity profile. The HDR images are taken at different exposure settings ranging from 120 μs to 12 s with 3 shots for every exposure setting. I take a moving standard deviation with 10 pixels to quantify the local fluctuations in the intensity profile of the primary beam. I obtain a maximum (positive amplitude) standard deviation of 2.19 dB from the smoothed trend and a peak intensity fluctuation of 5.68 dB measured from different shots.

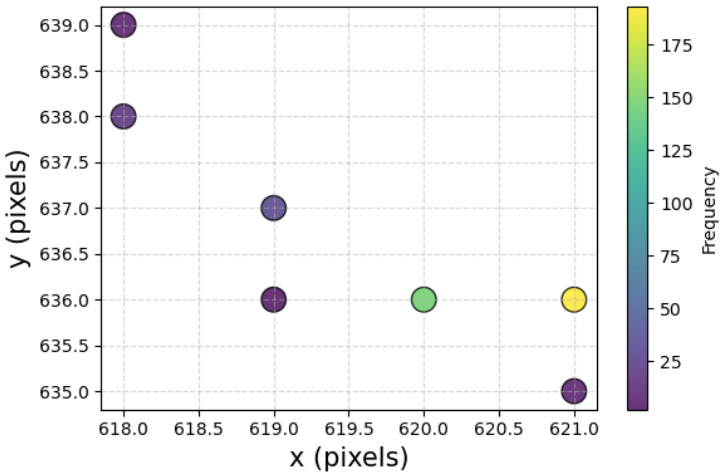


Figure 3.13: Plot showing different beam locations as seen on the camera at IP1 for different data points in the 2D scan shown in Figure 3.11. The color map shows the frequency of occurrence for a particular beam center location.

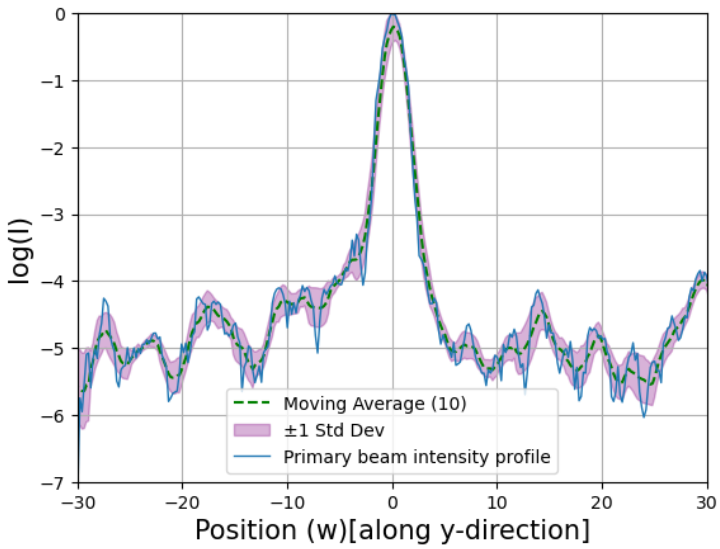


Figure 3.14: Figure showing the actual intensity profile of the primary beam, with the moving average/smoothened curve with 10 pixels. The shaded pink region shows the estimated maximum and minimum fluctuations in the intensity.

3.5 Summary and Discussion

In summary, the secondary grating method has successfully established its functionality by locally reducing the intensity crosstalk at the neighboring ion location ($4w_{\mathrm{IP1}}$) at the intermediate image plane IP1. I see a net suppression of I_X by ≈ 6 dB using this method for optimized values of the phase (ϕ_2) and amplitude (A_2') parameters. Using the same methodology, the idea can be extended to any ion location, all the way to the Ion plane with suitable relay optics. Successful relay of the intensity crosstalk suppression to the Ion plane will significantly improve the preservation fidelity of asset qubits while measuring the process qubit from 99.6% [44] to 99.9%.

Chapter 4

DMD as a Double Pass

Author's Contributions: The idea of using an intermediate image plane filter for the addressing beam was developed in discussions with Prof. Rajibul Islam. Dr. Chung-You (Gilbert) Shih suggested the idea of reusing the DMD for this purpose. The execution of the idea, involving development of the experimental setup and the data extraction, has been contributed by the author, who benefited from discussions with Prof. Rajibul Islam.

4.1 Overview

The Bloodstone processor will be used to trap and control a chain of over 30 ions, with an addressable region spanning approximately 200 μm. The intensity crosstalk (I_X) reaches an asymptotic value of 10^{-4} as we move further away (generally after the third or fourth nearest neighbor) from the center of the addressing beam along the ion-chain when using IFTA for hologram generation (See Section 2.4), which makes the system susceptible to long-range errors during MCMR cycles. This may lead to a constant propagation of errors after a certain location in the ion chain, thus increasing the total measurement error in the system.

Let us consider a chain of n ions, and each asset ion is exposed to the same intensity crosstalk of $I_{x,i} \approx 10^{-4}$. From Ref. [44], $I_X = 10^{-4}$ corresponds to $P_{\text{AQM}} \approx 10^{-3}$. Therefore, the measurement error corresponding to the i-th qubit is given by $P_{\text{AQM},i} = 10^{-3}$. Thus, the net measurement error in the ion chain is $\sum_n P_{\text{AQM},i} \approx n \times P_{\text{AQM}}$. For a chain of 30 ions, the net measurement error will be an order of magnitude worse $\sum_{30} P_{\text{AQM},i} \approx 10^{-2}$, thus decreasing the net fidelity by $\approx 1\%$. Hence, having a lower asymptotic value of I_X as

we move further away from the process qubit may help us to reduce the total measurement error in the system. To address this, a strategy has been suggested to use an intermediate image plane filter to cut down the I_X further away from the process qubit location.

I utilize the DMD to serve as the intermediate image plane pupil, in addition to generating the hologram. This is attributed to its dynamic control and fast switching time. The double pass method has shown promising results by lowering I_X to 10^{-6} beyond $x = 14w$, i.e., beyond the third nearest neighbor. This can significantly improve the cumulative measurement fidelity for a long chain of ions and thus help mitigate long-range measurement errors.

This method can also be extended to other MCMR architectures where long-range errors, due to a global measurement beam, affect the measurement fidelity of asset/auxiliary qubits, as seen in Ref. [40]. This emphasizes the engineering of an efficient, low-crosstalk individual addressing beam to perform MCMR operations.

All results presented in this chapter are measured at an intermediate image plane using a camera, and can be extended to the ion plane through appropriate de-magnification.

4.1.1 Chapter Outline

The chapter outline is given as follows:

- In Section 4.1, I give a brief overview of the research problem and introduce the DMD as a double pass method.
- In Section 4.2, I give a simplified picture of the key idea behind the method and provide the theoretical understanding.
- In Section 4.3, I discuss the experimental setup for the method, along with a discussion about the engineering challenges. A short description of the methodology is also provided.
- In Section 4.4, I give the key results obtained using the method. This includes aberration characterization and calibration of the beam location at the Image Plane 1 (IP1). I study the effect of different pupil sizes at IP1 on the resultant beam at Image Plane 2 (IP2).
- In Section 4.5, I summarize the chapter and reiterate the main results obtained in terms of reduced I_X and discuss how it will help us in mitigating long-range errors.

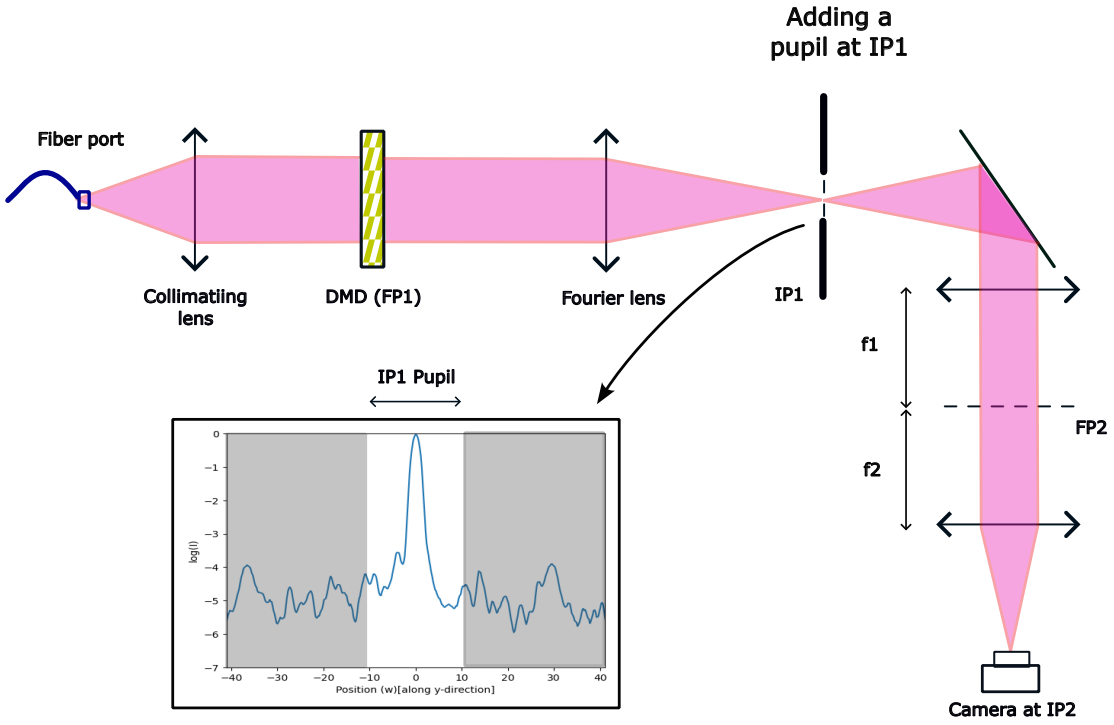


Figure 4.1: A simplified schematic presenting the idea of using a pupil to act as a filter at the intermediate image plane (IP1). This pupil is used to essentially block the asymptotic tail of the Gaussian distribution of the intensity of the addressing beam, thus reducing I_X outside the region of the pupil. DMD has been shown as a transmissive element for simplicity.

4.2 Theoretical Background

The idea behind DMD as a double pass can be visualized by looking at a simplified picture given in Figure 4.1. A primary grating is supplied to the DMD to create a Gaussian beam with waist, w. A sharp pupil is placed at the intermediate image plane, i.e., Image Plane 1 (IP1), with size d centered around the first-order beam. The pupil acts as an aperture function given as,

$$A_{\mathrm{IP1}}(x) = \begin{cases} 0 & \text{for } x > d/2 \text{ and } x < -d/2, \\ 1 & \text{for } -d/2 \leq x \leq d/2. \end{cases} \tag{4.1}$$

The resultant electric field at the IP1 after adding the pupil is given by,

$$E'_{\mathrm{IP1}}(x) = A_{\mathrm{IP1}}(x) \times E_{\mathrm{IP1}}(x), \tag{4.2}$$

$$= \begin{cases} 0 \text{ for } x > d/2 \text{ and } x < -d/2, \\ E_{\mathrm{IP1}}(x) \text{ for } -d/2 \leq x \leq d/2, \end{cases} \tag{4.3}$$

where $E_{\mathrm{IP1}}(x)$ is the electric field corresponding to the first-order beam (without any aperture) at the IP1.

IP1 (Image Plane 1) is imaged at IP2 (Image Plane 2) using a telecentric imaging system consisting of two lenses with focal lengths f_1 and f_2, with a magnification equal to $\frac{f_2}{f_1}$. Under diffraction-limited conditions, the electric field at IP2 will have the nature as in Equation 4.2 with the intensity outside the region of the pupil given by the background noise floor. Due to the finite aperture of the optics in the relay to IP2, we do not achieve diffraction-limited performance, which means the resultant electric field in IP2 has an effective aperture (d') that differs from the one set by the pupil size (d).

To accommodate the entire ion chain, we need a pupil with dynamic control over the position and also fast switching times (> 10 kHz), which are comparable to the switching time of the DMD generating the hologram. Hence, a clever idea to use a DMD as the pupil is employed. This is done by turning on a small subset of mirrors, which act as a reflective pupil. The location and the size of the pupil can be controlled by choosing the location and number of mirrors to turn on. Since the effective Fourier plane displaying the hologram is smaller than the physical aperture of the DMD, the unused DMD plane can be reused. So, the light is bent back to the DMD such that the DMD is physically both at the Fourier plane and the IP1, with different regions of the DMD surface responsible for hologram generation and the pupil, respectively.

4.3 Experimental set-up

4.3.1 Optical Schematic

The optical schematic for the method has been shown in Figure 4.2. A Polarization Maintaining (PM) fiber serves as the input source to the setup. The light is collimated using a 75 mm lens to get a beam with a waist, 5 mm. A Polarizing Beam Splitter (PBS) cube on a rotation mount acts as the polarizer. Two bending mirrors are added before the DMD, and the angle of incidence to the DMD is adjusted to match the blazing condition. Blazing

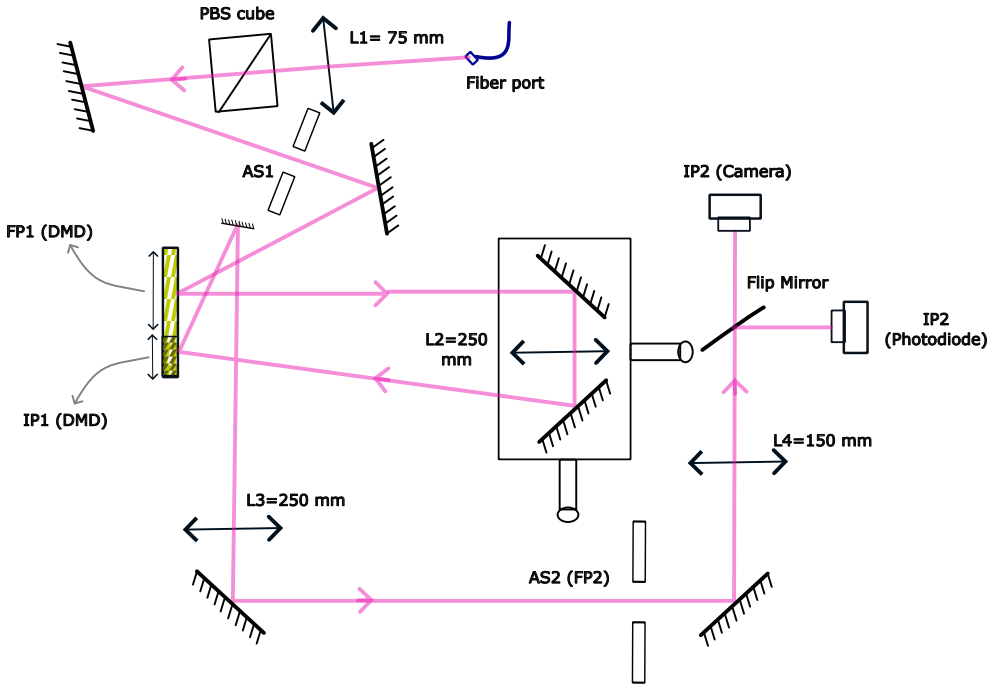


Figure 4.2: Optical Schematic for the DMD as a Double Pass method. The DP retro-reflector board is placed on a stage to control the location of IP1. AS1 and AS2 refer to Aperture Stop 1 and 2, respectively. The size of the DMD is not to scale for more clarity.

condition refers to an optimized incident angle to the DMD such that the diffraction efficiency is maximized [48]. The engineered wavefront reflected off the DMD is retro-reflected using the DP retro-reflector board (See Figure 4.4) with a 250 mm lens as the Fourier lens. The angle of the second mirror in the DP retro-reflector board is adjusted to make the beam fall on the IP1 region of the DMD. A D-shaped mirror is used to reflect the first-order beam. This is to make sure that the mirror does not block the incoming beam falling on the FP1 region of the DMD. A telecentric imaging system with focal lengths of 250 mm and 150 mm is used to image IP1 at IP2. A CMOS camera (FLIR BFS-PGE-120S4M-CS) is placed at the IP2 to image the beam which is supposed to get relayed to the ion plane. A flip mirror is added before the camera to have the alternative of using a photodiode at the IP2.

4.3.2 Engineering Challenges

Using the DMD in a double pass configuration presents engineering challenges due to the configuration of the micro mirrors (ON/OFF direction), the small aperture of the DMD, the optical separation of the Fourier plane from the IP1, and diffraction from the micro mirrors at the pupil at IP1. The following approaches were implemented to address the identified challenges:

Input beam iris

The size of the DMD chip is 2560 × 1600 pixels (19.5 mm × 12.1 mm). The length of the Fourier plane (FP1) is defined from 0 to 1960 pixels, and the Image plane (IP1) length is defined from 2060 to 2560 pixels with 100 pixels in between acting as a buffer (shown in Figure 4.3). The input beam falling on the FP1 region of the DMD needs to be optically separated from the IP1 region of the DMD. This is done by incorporating a 3D printed iris (Figure 4.3) before the light falls on FP1 region of the DMD. The size of the iris is chosen such that it's large enough to illuminate FP1 without illuminating IP1. The location of the beam can be fine adjusted using the adjustable mirror before the DMD.

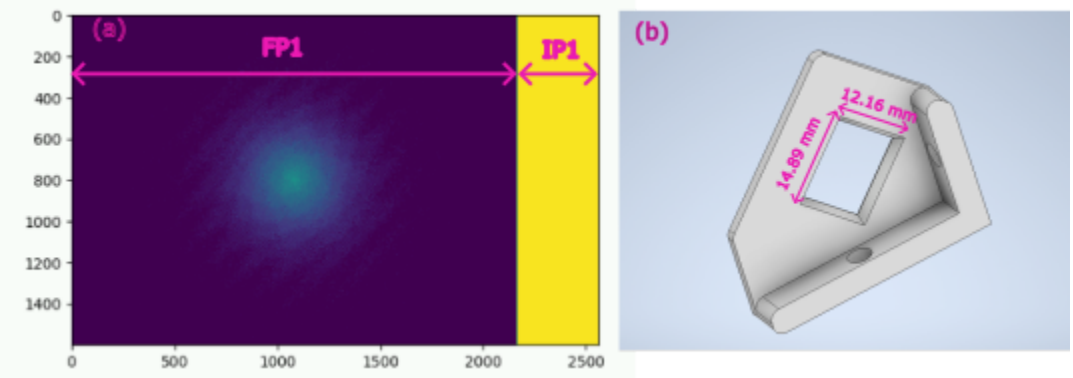


Figure 4.3: (a) Demarcation between the FP1 [0, 2060] (the 100 pixels buffer is included here) region and IP1 [2060, 2560] region of the DMD is shown. (b) A 3D printed iris for optical separation of the input beam to FP1 from IP1. The size of the iris is chosen to match the dimensions of FP1.

Retro-reflective DP board

A board is machined as shown in Figure 4.4, which acts as the retro-reflector. The board consists of the Fourier lens (250 mm) sandwiched between two bending mirrors. This board ensures that the Fourier lens is equidistant from both the FP1 and the IP1. The board is mounted to a stage to control the relative distances to the DMD. The mirror after the Fourier lens can be adjusted to make the beam fall on the IP1 region of the DMD. The beam is aligned to the DMD by turning on all the mirrors at IP1 (DMD) and observing the reflected beam.

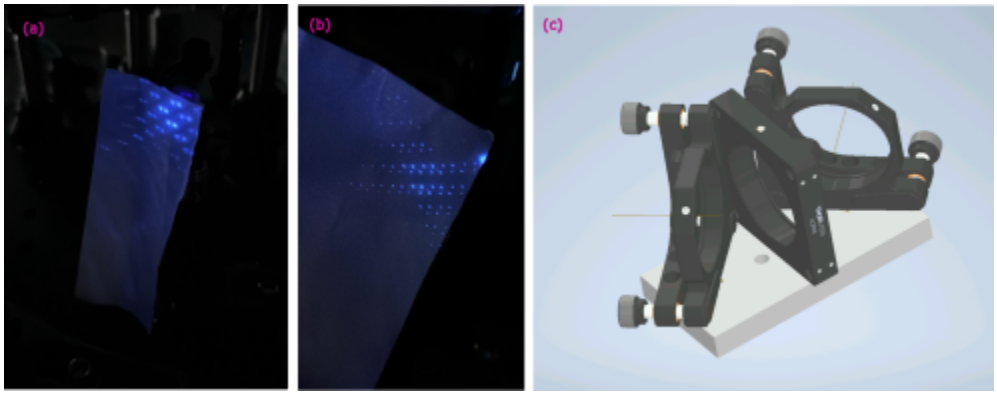


Figure 4.4: (a) Image of the first and zeroth order Gaussian beam reflected from the IP1 (DMD) for a particular amplitude grating hologram. (b) Image of the first and zeroth orders for two patches turned on at the center reference and at some other point in the grid. The multiple diffraction orders seen in (a) and (c) are a result of diffraction effects from the natural grating of the micro mirrors in the DMD. (c) DP (Double Pass) retro-reflector board: A board machined to serve as a retro-reflector with the Fourier lens sandwiched in between two bending mirrors.

Separation of diffraction orders

The DMD micro mirrors alternate between $\pm 12°$. This means for a zero angle of incidence to the plane of the DMD, the light is reflected by $24°$. After the double pass, the reflected light bends towards the input beam; hence, a D-shaped mirror is used to reflect the beam out of the way. The natural grating of the DMD created due to the finite size of the micro mirrors creates several diffraction orders. The presence of the diffraction orders helps us to distinguish the beam reflected off the micro mirrors from the beam reflected off the glass

window. A suitable diffraction order is chosen based on the power efficiency/brightness. It is important to separate out the unwanted diffraction orders to get rid of unwanted features in the IP2. This is especially important during aberration characterization, which relies on the interference of two plane waves, where the presence of any extra beams can pollute the fringe profile. This can lead to incorrect extraction of the resultant phase. I tackle this issue by filtering out the unwanted order at the intermediate Fourier plane (FP2) between L2 and L3 as shown in Figure 4.5. This is done with the help of an adjustable iris.

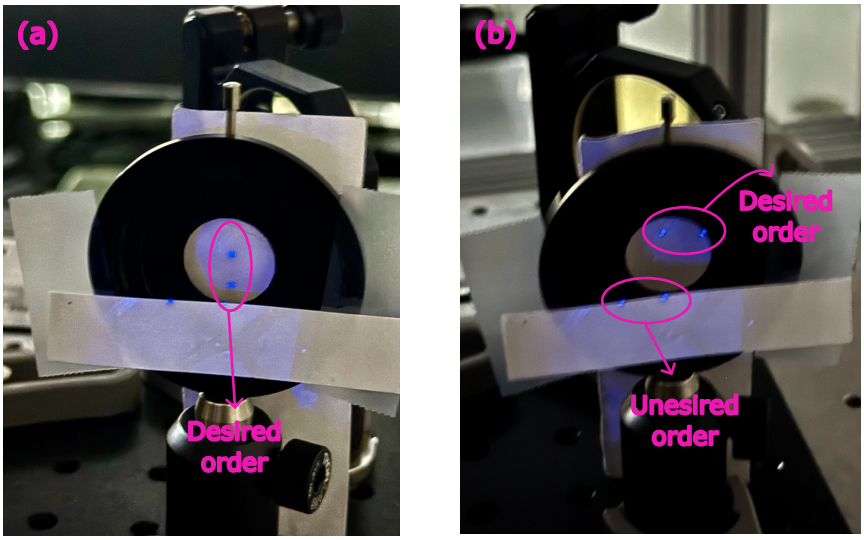


Figure 4.5: (a, b) An iris is used at the FP2 to filter out the beam from the undesired orders. The size of the iris has to be adjusted such that the light reflected from the scanning patch of the desired order can make it through the iris while blocking the other beams corresponding to the undesired orders.

4.3.3 Methodology

The methodology used for the DMD as a Double Pass method is described as follows:

- An aberration-corrected Gaussian beam profile with a waist w is generated at the IP1, and all the mirrors are turned on at the IP1 (DMD).
- The location of the beam on IP1 (DMD) is verified by scanning a small subset of micro mirrors where the beam is expected to fall. This is accomplished by turning

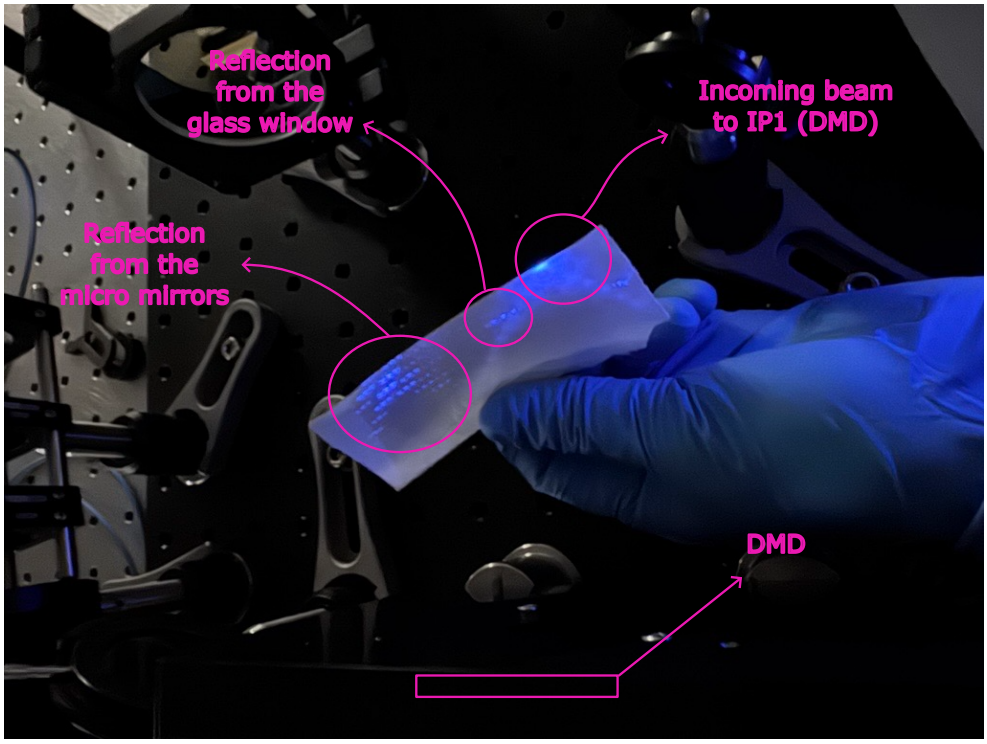


Figure 4.6: This picture gives a relative idea about the direction of the incoming beam, reflection from the protective glass window on the DMD and the reflection from the micro mirror array.

on individual mirrors at IP1 and monitoring the corresponding photodiode signal at IP2.

- Once the location of the center of the beam falling on the IP1 (DMD) is known, specific number of mirrors can be turned on to imitate a pupil of size $d = n \times px$ (Here px refers to the size of each DMD micro mirror and is given by 7.6 μm) and an HDR image is taken at IP2.

4.4 Results: Measurement of Intensity Crosstalk

4.4.1 Aberration Data

The aberration characterization is done in three steps for this setup. I first characterize the aberration until IP1 [$\Phi_0(x)$ and $\Phi_1(x)$]. This is done by putting a bending mirror before the beam goes back to the DMD and placing a camera at the new IP1. The remainder of the aberration coming from the telecentric imaging system, $\Phi_2(x)$ is characterized using $\Phi_0(x) + \Phi_1(x)$ as the feedback. The iris at FP2 needs to be suitably adjusted such that the undesired diffraction orders are blocked, at the same time the entire grid of scanning patches passes through. The size of the Fourier plane chosen for characterizing $\Phi_0(x)$, $\Phi_1(x)$ and $\Phi_2(x)$ is 1600 pixels, 1480 pixels and 1430 pixels, respectively.

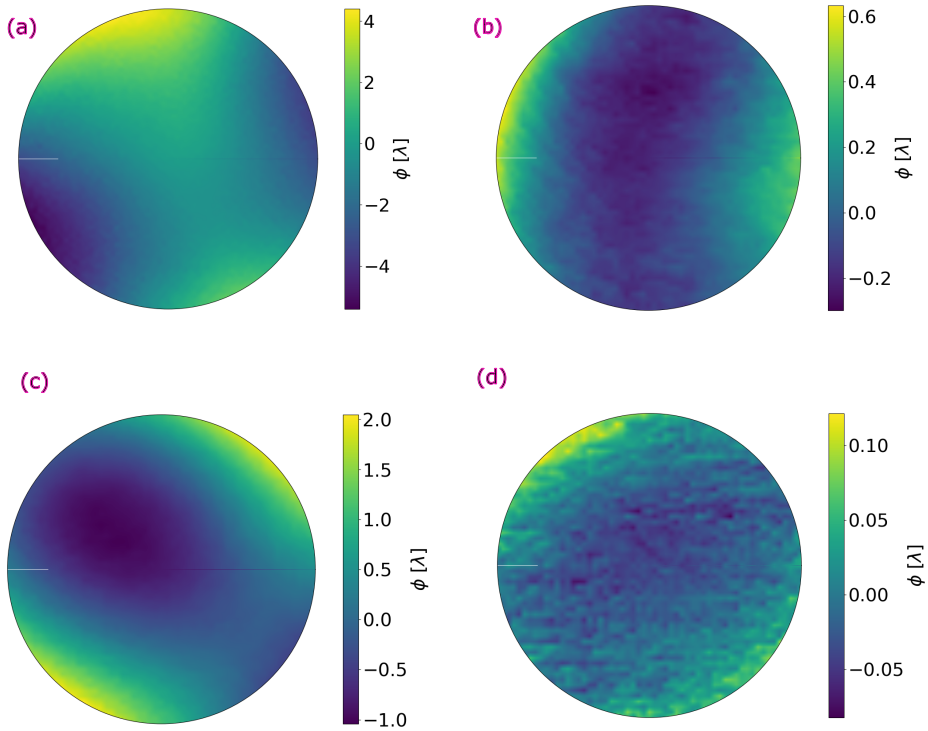


Figure 4.7: (a, b, c) Aberration maps corresponding to $\Phi_0(x)$, $\Phi_1(x)$ and $\Phi_2(x)$ respectively. (d) This is the residual aberration map obtained after compensating for the aberrations using $\Phi_0(x) + \Phi_1(x) + \Phi_2(x)$. (Radius of the Fourier plane is 700 pixels)

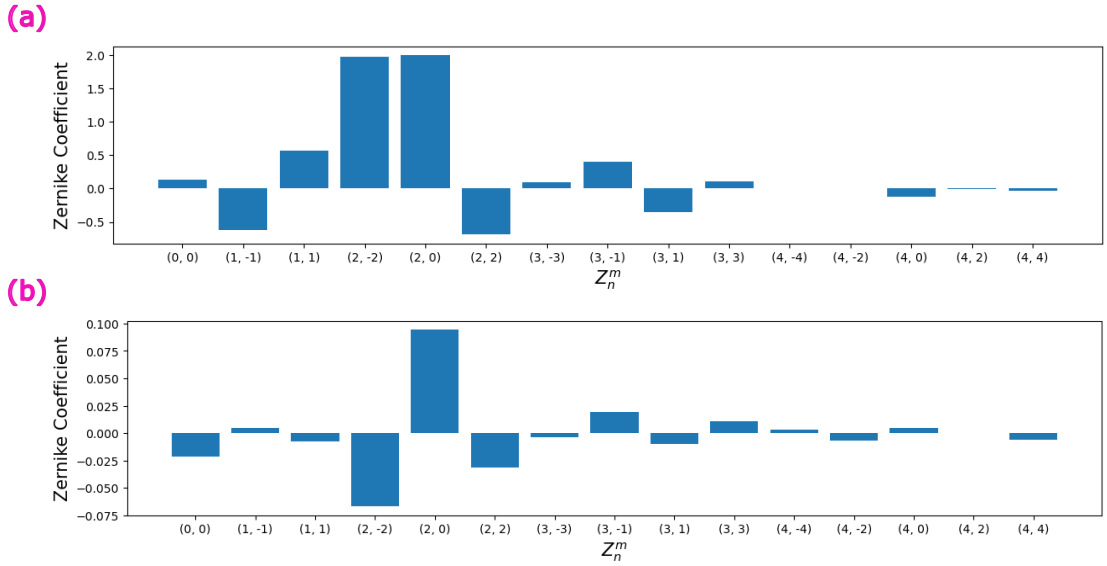


Figure 4.8: Figure showing Zernike decomposition of (a) $\Phi_2(x)$ and (b) the residual phase map obtained after aberration compensation. This is obtained by mapping the phase maps to Zernike polynomials, which are a sequence of polynomials orthogonal in nature and defined on a unit circle. The x-axis denotes the Zernike polynomials (Z_n^m) corresponding to different aberration types, while the y-axis shows their coefficients, indicating the strength of each aberration. The dominant aberrations are astigmatism [(2,-2),(2,2)] and defocus [(2,0)] for both (a) and (b).

$\Phi_2(x)$ is measured to be 4.35λ (8.7π) peak-to-peak and 0.96λ RMS (Figure 4.7). Most of the aberration in $\Phi_2(x)$ is dominated by astigmatism and defocus (See Figure 4.8). Even after compensation, the dominant aberration is defocus, which arises due to the configuration of the micro mirrors since they do not form a continuous plane at the ON state, i.e., when all the mirrors are turned on at the IP1. Thus, for different ion locations, the aberration profiles will be different. After compensating for all the aberrations [$\Phi_0(x) + \Phi_1(x) + \Phi_2(x)$], I get a residual aberration of 0.14λ (0.28π) peak-to-peak and 0.02λ RMS.

4.4.2 Beam Location Calibration

The center of the beam falling on the IP1 (DMD) needs to be calibrated. An estimate could be made for the subset of micro mirrors on which the beam center would lie. This can be done by doing a simple binary search. A 20×20 grid is determined this way. The

exact location of the center of the beam is verified by doing a linear scan where each mirror in the 20×20 grid is turned on and the corresponding signal is recorded at the IP2 with the help of an avalanche photo diode (APD). The center of the beam is determined from the micro mirror corresponding to the highest voltage. An insight into the shape of the beam at IP1 can also be obtained from the voltage plot (Figure 4.9), which seems to be aberrated by $\Phi_2(x)$ as compared to IP2.

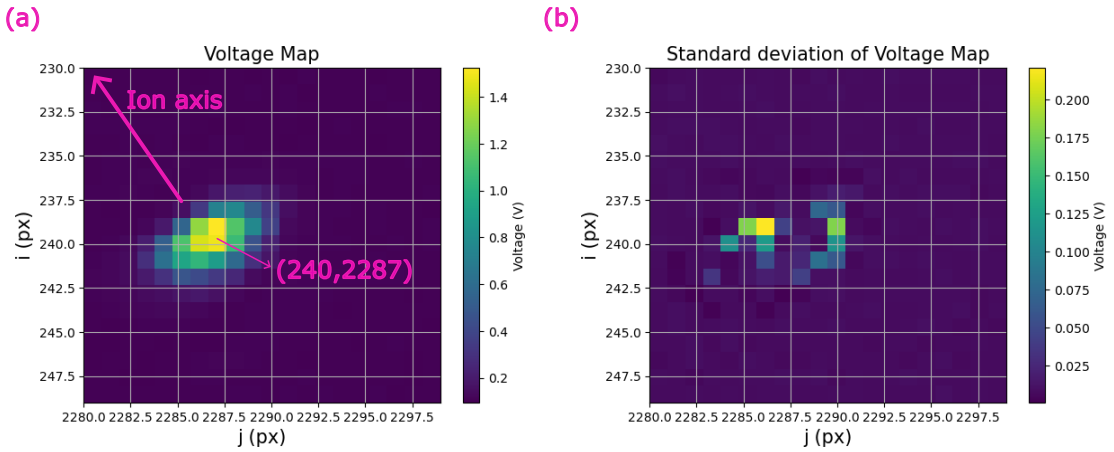


Figure 4.9: (a) Figure showing the voltage signal (10 shots) as seen on an oscilloscope connected to the output of the photodiode at the IP2, as micro mirrors are turned on, one at a time in a selected 20×20 grid at the IP1 (DMD). The gain of the photodiode is set to maximum to obtain best signal-to-noise ratio. Here, the maximum voltage corresponds to 1.5 V with a background noise of 0.09 V. (b) The standard deviation map for different shots is plotted with a maximum standard error of 0.07 V.

4.4.3 Intensity Crosstalk Data

An aberration compensated Gaussian beam with waist $w_{\text{IP1}} = 15\ \mu$m is created using IFTA at the IP1. When all mirrors are turned on at IP1, after suitable de-magnification from the telecentric imaging system ($\frac{f_2}{f_1} = \frac{150}{250} = \frac{3}{5}$), a Gaussian beam with waist $w_{\text{IP2}} = 9\ \mu$m is created at IP2. The size of each micro mirror is 7.6 μm which is $\approx w_{\text{IP1}}/2$. The center of the beam falling on the IP1 (DMD) is determined using the method suggested in Subsection 4.4.2. A comparison can be drawn at the effect of the intermediate pupil at IP2 from the Figure 4.10. An effective aperturing of size d' can be seen from the IP1 pupil (d). The intensity crosstalk (I_X) falls from 10^{-4} to 10^{-6} outside the effective aperture. $I_X = 10^{-6}$

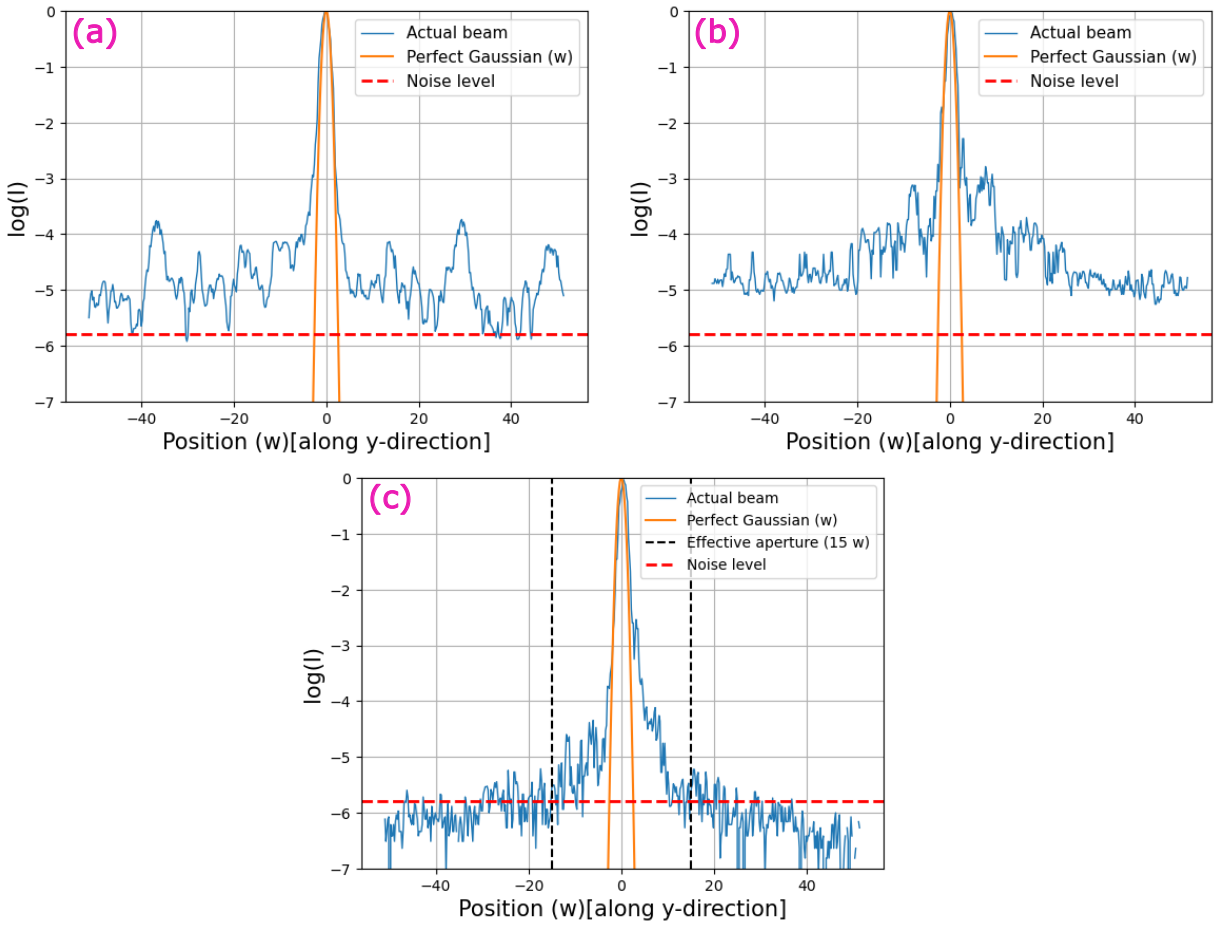


Figure 4.10: (a) HDR image of a Gaussian beam when DMD is used as a single pass. (b) HDR image of a Gaussian beam when the DMD is used as double pass and all the mirrors are turned on at the IP1 (infinite pupil). There is an increase in noise compared to (a) due to scattering from the configuration of the micro mirrors in the DMD, which do not form a single continuous plane (c) HDR image of a Gaussian beam when the DMD is used as a double pass and the IP1 pupil size is set to $2w$. Here, the y-direction corresponds to the direction along the ion chain, and w is the waist of the addressing/probe beam. Noise level refers to the maximum background intensity when the addressing/probe beam is turned off.

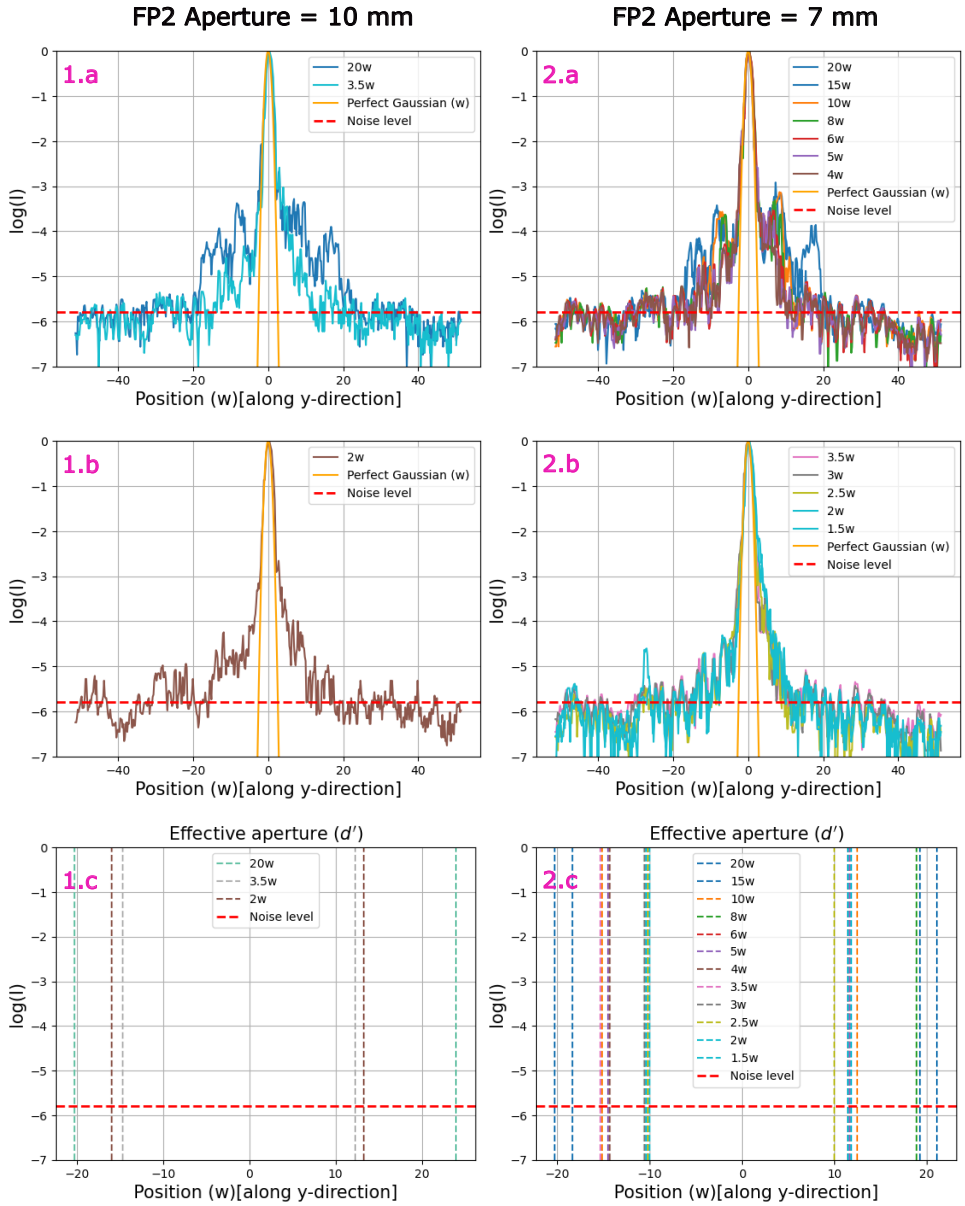


Figure 4.11: 1. FP2 iris is set to a diameter of 10 mm, i.e., maximum Fourier plane aperture and 2. FP2 iris is set to 7 mm (1.a, 1.b, 2.a, 2.b) HDR images taken for varying pupil size $1.5w \leq d \leq 20w$. (1.c, 2.c) Corresponding effective aperture (d') for different pupil sizes (d). Here, the y-direction corresponds to the direction along the ion chain, and w is the waist of the addressing/probe beam. Noise level refers to the maximum background intensity when the addressing/probe beam is turned off.

also corresponds to the noise floor intensity threshold when there is no light going to the camera. Thus, this method can be used to cut down I_X in a long chain of ions and help diminish long-range measurement errors.

The effect of IP1 pupil size (d) on the effective aperture (d') can be further studied as shown in Figure 4.11. The effective aperture (d') appears to decrease with the decrease in IP1 pupil size (d) as it is varied from $20w_{\text{IP1}}$ to $1.5w_{\text{IP1}}$.

There seemed to be some scattered light around the center of the beam coming from the DMD, which was verified by comparing the shape of the beam falling on the DMD with the one at IP2. This could be attributed to some scattering within the micro mirror array. To cut down the scattering, I adjust the FP2 iris (FP2 refers to the intermediate Fourier plane (FP) in the $f_1 + f_2$ telecentric imaging system as shown in Figure 4.1) from a diameter of 10 mm to $\approx$ 7 mm until I could visibly reduce some of the noisy peaks around the beam center. I study the effect of changing IP1 pupil sizes (d) for both cases, i.e., FP2 aperture of 10 mm and 7 mm, respectively. The minimum effective aperture was obtained to be, $10w \leq d'_{\text{min}} \leq 14w$. This was calculated by smoothing the trend of the data, considering a window size of 5 data points (pixels). Thus, a significant reduction of I_x was obtained beyond $14w$, which corresponds to a location beyond the third nearest neighbor from the probe beam location.

Table 4.1: Average effective aperture $d'(w)$ for different FP2 apertures

IP1 pupil size $d(w)$	**FP2 Aperture = 10 mm** $d'(w)$	**FP2 Aperture = 7 mm** $d'(w)$
20	22.14	20.70
15	-	18.85
10	-	13.80
8	-	14.73
6	-	10.92
5	-	13.08
4	-	12.87
3.5	13.49	13.39
3	-	11.02
2.5	-	10.09
2	14.62	10.71
1.5	-	11.12

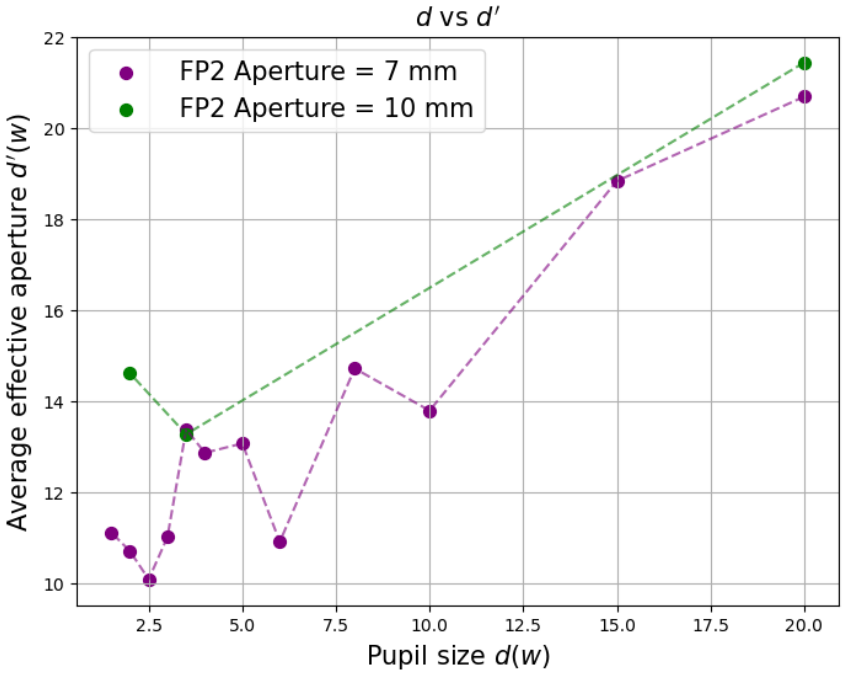


Figure 4.12: Comparison of effective aperture ($d'(w)$) for different sizes of IP1 pupil ($d(w)$) for FP2 apertures of 7 mm and 10 mm, respectively. A linear decrease in the effective aperture ($d'(w)$) can be seen with a decrease in IP1 pupil sizes ($d(w)$).

4.4.4 Error Analysis

All the data is in terms of HDR images taken at different exposure settings ranging from 120 μs to 12 s. I took 3 shots for every exposure setting. The shot-to-shot variation for each HDR image can be seen in Figure 4.13. The peak-to-peak fluctuation in the intensity noise is also characterized in Figure 4.13. The maximum fluctuation in noise is 4 dB, and the maximum standard error is 1 dB.

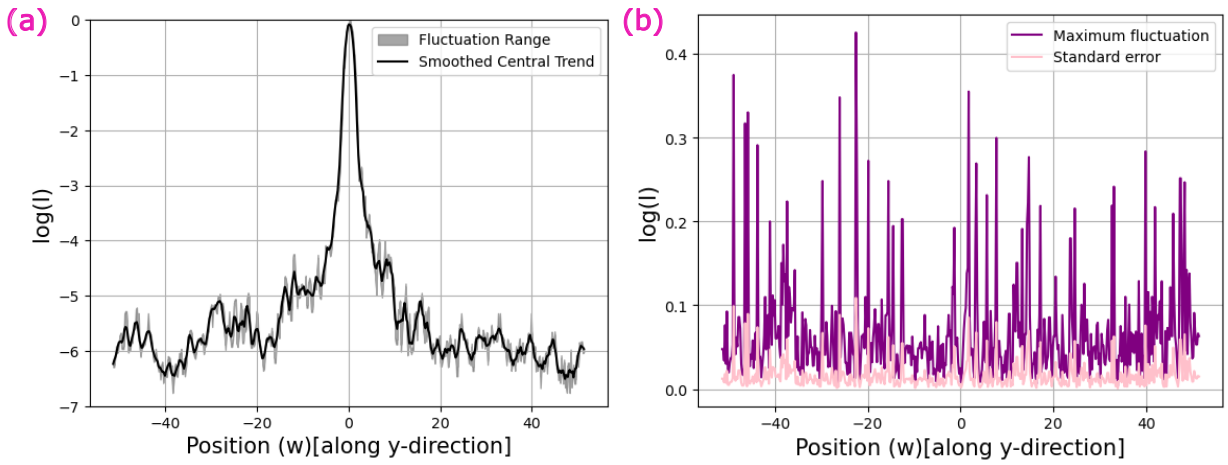


Figure 4.13: (a) Shot-to-shot intensity fluctuation in the HDR images taken for a single data (b) Plot showing maximum (peak-to-peak) fluctuation and standard error at each point. Maximum peak-to-peak fluctuation is 4 dB, and maximum standard error is 1 dB.

4.5 Summary and Conclusion

In this chapter, an innovative approach was suggested to mitigate long-range intensity crosstalk (I_X) from an individual addressing probe beam. The DMD as a double pass method is based on the idea of filtering out the tail of a Gaussian beam using the DMD again at the intermediate image plane. Using this method, I have successfully reduced I_X from 10^{-4} to 10^{-6} beyond $14w_{\mathrm{IP1}}$, which corresponds to a location beyond the third nearest neighbor in the ion chain. In this setup, the observed crosstalk is currently limited by the background noise threshold, i.e., 10^{-6}, suggesting that the true I_X could be even lower with improved background noise.

This method represents a significant improvement from the previous methods in terms of mitigation of long-range intensity crosstalk and can help reduce long-range measurement errors in a long ion chain. This reduction in I_x at the asymptotic limit when successfully relayed to the ion plane will improve the total measurement error in a long chain (> 10) of ions from $\approx 10^{-3}$ to $\approx 10^{-4}$. This architecture can also be extended to other techniques where long-range errors due to an inefficient addressing system can reduce the fidelity of mid-circuit measurements [40].

Chapter 5

Conclusion and Outlook

Over the years, trapped-ions have become a popular platform for both digital and analog quantum computation. Integrated features such as MCMR support the development of error-corrected systems and provide access to many near-term algorithms, thereby advancing the architecture towards fault tolerance. While different architectures exist to implement MCMR, this thesis presents optical engineering improvements in terms of reduced intensity crosstalk to using spatial modification of individual addressing beams to realize MCMR in ion-traps.

In summary, this thesis proposed two key improvements to the existing approach of using IFTA with an aberration-compensated beam for generating a low-crosstalk individual addressing beam. The two approaches explored were: 1. The secondary grating method, and 2. using the DMD in a double pass configuration.

I successfully demonstrated the implementation of the secondary grating method, achieving a reduction in absolute intensity crosstalk at the nearest neighbor location by ≈ 6 dB. This reduction in the intensity crosstalk is expected to improve the average measurement fidelity in the MCMR process, which has previously been shown to be limited by the preservation fidelity of ions lying between $4w$ and $20w$ [44], resulting from higher intensity crosstalk. With this method, the absolute intensity crosstalk can be suppressed to 50 dB at the nearest neighbor, thus bringing us near the regime set by the fundamental limit from inter-ion scattering. This technique can be used to locally mitigate the absolute intensity crosstalk at any arbitrary ion location in the chain and can also be potentially expanded to simultaneously mitigate the absolute intensity crosstalk at multiple ion locations with the help of multiple secondary gratings.

Using the DMD in a double-pass configuration, I was able to significantly reduce the

asymptotic limit of intensity crosstalk from the individual addressing beam to below 60 dB (10^{-6}), compared to the previously obtained level of 40 dB (10^{-4}) beyond $14w$. This substantial reduction will contribute to minimizing long-range measurement errors in the system and improving the total measurement fidelity. This is especially important considering several protocols use multiple cycles of MCMR where reducing this cumulative measurement error becomes important. This method presents certain engineering challenges in maintaining aberration compensation for beams targeting different ion locations, primarily due to the additional aberrations, such as defocus, introduced by the physical configuration of the DMD micro mirrors, which can be optimized further. The result corresponding to 60 dB is also limited by the background noise level as measured by the camera, which can be improved further.

As an outlook, these methods represent a significant improvement over existing techniques, thus advancing the architecture for using spatial modulation of light to perform MCMR in trapped-ion systems. The results presented in this thesis are only up to an intermediate image plane and can be relayed to the ions with suitable optics. Once integrated with ions, the techniques will offer deeper insight into their effectiveness in preserving measurement fidelities of asset qubits when probing process qubits using atomic physics techniques such as Ramsey interferometry, as used in Ref. [44], and can be used to benchmark against other MCMR techniques [40].

This engineering advancement opens up several new avenues of research. The reduction of absolute intensity crosstalk near the regime of fundamental limit at the neighboring ions will enable experimental investigation of inter-ion scattering rates, which have only been theoretically estimated so far. Improved preservation fidelity from reduced intensity crosstalk at the nearest neighbor will also reduce constraints on fast measurement times, which depend on high fidelity detection to maintain the same measurement fidelity. Similarly, reduced long-range intensity crosstalk will be helpful in improving total measurement fidelity in multiple cycles of MCMR, which is necessary in syndrome extraction in several error correction protocols and has been shown to be a bottleneck in a recent demonstration of Steane error correction code in trapped-ion qubits [57].

Thus, the optical engineering advancements proposed in this thesis have the potential to improve state-of-the-art mid-circuit measurement and reset fidelities in trapped-ion systems, thereby contributing to the development of a fault-tolerant quantum computing architecture.

References

[1] Peter W. Shor. Polynomial-time algorithms for prime factorization and discrete logarithms on a quantum computer. *SIAM Journal on Computing*, 26(5):1484–1509, October 1997. 1

[2] Vanessa C. Olaya-Agudelo, Ben Stewart, Christophe H. Valahu, Ryan J. MacDonell, Maverick J. Millican, Vassili G. Matsos, Frank Scuccimarra, Ting Rei Tan, and Ivan Kassal. Simulating open-system molecular dynamics on analog quantum computers. *Phys. Rev. Res.*, 7:023215, Jun 2025. 1

[3] Igor Gaidai, Dmitri Babikov, Alexander Teplukhin, Brian K. Kendrick, Susan M. Mniszewski, Yu Zhang, Sergei Tretiak, and Pavel A. Dub. Molecular dynamics on quantum annealers. *Scientific Reports*, 12(1):16824, 2022. 1

[4] Aram W. Harrow, Avinatan Hassidim, and Seth Lloyd. Quantum algorithm for linear systems of equations. *Phys. Rev. Lett.*, 103:150502, Oct 2009. 1

[5] Anton Robert, Panagiotis Kl. Barkoutsos, Stefan Woerner, and Ivano Tavernelli. Resource-efficient quantum algorithm for protein folding. *npj Quantum Information*, 7(1):38, 2021. 1

[6] Lov K. Grover. A fast quantum mechanical algorithm for database search, 1996. 1

[7] John Preskill. Quantum computing in the nisq era and beyond. *Quantum*, 2:79, 2018. 1

[8] Kishor Bharti, Alba Cervera-Lierta, Thi Ha Kyaw, Tobias Haug, Sumner Alperin-Lea, Abhinav Anand, Matthias Degroote, Hermanni Heimonen, Jakob S. Kottmann, Tim Menke, Wai-Keong Mok, Sukin Sim, Leong-Chuan Kwek, and Alán Aspuru-Guzik. Noisy intermediate-scale quantum algorithms. *Rev. Mod. Phys.*, 94:015004, Feb 2022. 1

[9] Richard P. Feynman. Simulating physics with computers. *International Journal of Theoretical Physics*, 21(6):467–488, 1982. 2

[10] Stefanie Czischek, Giacomo Torlai, Sayonee Ray, Rajibul Islam, and Roger G. Melko. Simulating a measurement-induced phase transition for trapped-ion circuits. *Phys. Rev. A*, 104:062405, Dec 2021. 2, 7

[11] Crystal Noel, Pradeep Niroula, Daiwei Zhu, Andrew Risinger, Laird Egan, Debopriyo Biswas, Marko Cetina, Alexey V. Gorshkov, Michael J. Gullans, David A. Huse, and Christopher Monroe. Measurement-induced quantum phases realized in a trapped-ion quantum computer. *Nature Physics*, 18(7):760–764, 2022. 2, 7

[12] A. Houck, H. Türeci, and J. Koch. On-chip quantum simulation with superconducting circuits. *Nature Physics*, 8(4):292–299, 2012. 2

[13] K. He, X. Geng, R. Huang, J. Liu, and W. Chen. Quantum computation and simulation with superconducting qubits. *Chinese Physics B*, 30(8):080304, 2021. 2

[14] Michael J. Hartmann. Quantum simulation with interacting photons. *Journal of Optics*, 18(10):Article 104005, 2016. 2

[15] Alán Aspuru-Guzik and Philip Walther. Photonic quantum simulators. *Nature Physics*, 8(4):285–291, 2012. 2

[16] C. Gross and I. Bloch. Quantum simulations with ultracold atoms in optical lattices. *Science*, 357(6355):995–1001, 2017. 2

[17] I. Aharonovich, A. D. Greentree, and S. Prawer. Diamond photonics. *Nature Photonics*, 5(7):397–405, 2011. 2

[18] C. Monroe, W. C. Campbell, L.-M. Duan, Z.-X. Gong, A. V. Gorshkov, P. W. Hess, R. Islam, K. Kim, N. M. Linke, G. Pagano, P. Richerme, C. Senko, and N. Y. Yao. Programmable quantum simulations of spin systems with trapped ions. *Rev. Mod. Phys.*, 93:025001, Apr 2021. 2

[19] R. Blatt and C. F. Roos. Quantum simulations with trapped ions. *Nature Physics*, 8(4):277–284, 2012. 2

[20] P. Wang, C. Luan, M. Qiao, M. Um, J. Zhang, Y. Wang, X. Yuan, M. Gu, J. Zhang, and K. Kim. Single ion qubit with estimated coherence time exceeding one hour. *Nature Communications*, 12(1):233, 2021. 2

[21] Sainath Motlakunta. *Developing a Large-Scale, Programmable Trapped Ion Quantum Simulator with In Situ Mid-Circuit Measurement and Reset.* PhD thesis, University of Waterloo, 2023. 3, 6

[22] Nikhil Kotibhaskar. Design and construction of an ion trapping apparatus for quantum simulation experiments. Master's thesis, University of Waterloo, 2019. 4

[23] S. Earnshaw. On the nature of the molecular forces which regulate the constitution of the luminiferous ether. *Transactions of the Cambridge Philosophical Society*, 7:97, 1848. 2

[24] W. Paul and H. Steinwedel. Ein neues massenspektrometer ohne magnetfeld. *Zeitschrift für Naturforschung A*, 8(7):448–450, July 1953. 2

[25] Klaus Mølmer and Anders Sørensen. Multiparticle entanglement of hot trapped ions. *Physical Review Letters*, 82(9):1835–1838, March 1999. 4

[26] Chung-You Shih, Sainath Motlakunta, Nikhil Kotibhaskar, Manas Sajjan, Roland Hablützel, ..., and Rajibul Islam. Reprogrammable and high-precision holographic optical addressing of trapped ions for scalable quantum control. *npj Quantum Information*, 7:57, April 2021. Open access; Published 8 April 2021. 6, 8, 9, 16, 17, 28, 37

[27] Nikhil Kotibhaskar. *Towards Large Scale Quantum Simulations with Trapped Ions: Programmable XY model, Precise Light Sensing, and Extreme High Vacuum.* PhD thesis, University of Waterloo, 2024. 6

[28] X. Mi, A. A. Michailidis, S. Shabani, K. C. Miao, P. V. Klimov, and J. Lloyd et al. Stable quantum-correlated many-body states through engineered dissipation. *Science*, 383(6689):1332–1337, 2024. 7

[29] C. Ryan-Anderson, J. G. Bohnet, K. Lee, D. Gresh, A. Hankin, J. P. Gaebler, D. Francois, A. Chernoguzov, D. Lucchetti, N. C. Brown, T. M. Gatterman, S. K. Halit, K. Gilmore, J. A. Gerber, B. Neyenhuis, D. Hayes, and R. P. Stutz. Realization of real-time fault-tolerant quantum error correction. *Phys. Rev. X*, 11:041058, Dec 2021. 7

[30] Matthew DeCross, Eli Chertkov, Megan Kohagen, and Michael Foss-Feig. Qubit-reuse compilation with mid-circuit measurement and reset. *Phys. Rev. X*, 13:041057, Dec 2023. 7

[31] P. O. Schmidt, T. Rosenband, C. Langer, W. M. Itano, J. C. Bergquist, and D. J. Wineland. Spectroscopy using quantum logic. *Science*, 309(5735):749–752, 2005. 8

[32] K. Singh, C. E. Bradley, S. Anand, V. Ramesh, R. White, and H. Bernien. Mid-circuit correction of correlated phase errors using an array of spectator qubits. *Science*, 380(6651):1265–1269, 2023. 8

[33] J. M. Pino, J. M. Dreiling, C. Figgatt, J. P. Gaebler, S. A. Moses, M. S. Allman, C. H. Baldwin, M. Foss-Feig, D. Hayes, K. Mayer, C. Ryan-Anderson, and B. Neyenhuis. Demonstration of the trapped-ion quantum ccd computer architecture. *Nature*, 592(7853):209–213, 2021. 8

[34] Daiwei Zhu, Gregory D. Kahanamoku-Meyer, Laura Lewis, Crystal Noel, Or Katz, Bahaa Harraz, Qingfeng Wang, Andrew Risinger, Lei Feng, Debopriyo Biswas, Laird Egan, Alexandru Gheorghiu, Yunseong Nam, Thomas Vidick, Umesh Vazirani, Norman Y. Yao, Marko Cetina, and Christopher Monroe. Interactive cryptographic proofs of quantumness using mid-circuit measurements. *Nature Physics*, 19(11):1725–1731, 2023. 8

[35] S. A. Moses and C. H. et al Baldwin. A race-track trapped-ion quantum processor. *Phys. Rev. X*, 13:041052, Dec 2023. 8

[36] Dolev Bluvstein, Harry Levine, Giulia Semeghini, Tout T. Wang, Sepehr Ebadi, Marcin Kalinowski, Alexander Keesling, Nishad Maskara, Hannes Pichler, Markus Greiner, Vladan Vuletić, and Mikhail D. Lukin. A quantum processor based on coherent transport of entangled atom arrays. *Nature*, 604(7906):451–456, 2022. 8

[37] Zuo-Yao Chen, Isabella Goetting, George Toh, Yichao Yu, Mikhail Shalaev, Sagnik Saha, Ashish Kalakuntla, Harriet Bufan Shi, Christopher Monroe, Alexander Kozhanov, and Crystal Noel. Non-invasive mid-circuit measurement and reset on atomic qubits, 2025. 8

[38] Yichao Yu, Keqin Yan, Debopriyo Biswas, Vivian Ni Zhang, Bahaa Harraz, Crystal Noel, Christopher Monroe, and Alexander Kozhanov. In-situ mid-circuit qubit measurement and reset in a single-species trapped-ion quantum computing system, 2025. 8

[39] J. P. Gaebler, C. H. Baldwin, S. A. Moses, J. M. Dreiling, C. Figgatt, M. Foss-Feig, D. Hayes, and J. M. Pino. Suppression of midcircuit measurement crosstalk errors with micromotion. *Phys. Rev. A*, 104:062440, Dec 2021. 8

[40] Daniel Hothem, Jordan Hines, Charles Baldwin, Dan Gresh, Robin Blume-Kohout, and Timothy Proctor. Measuring error rates of mid-circuit measurements. *Nature Communications*, 16(1):5761, 2025. 8, 19, 49, 64, 66

[41] J. Chiaverini, R. B. Blakestad, J. Britton, J. D. Jost, C. Langer, D. Leibfried, R. Ozeri, and D. J. Wineland. Surface-electrode architecture for ion-trap quantum information processing. *Quantum Information and Computation*, 5(6):419–439, 2005. 8

[42] J. H. Wesenberg. Electrostatics of surface-electrode ion traps. *Physical Review A*, 78(6):063410, 2008. 8

[43] Shuqi Xu, Xiaoxing Xia, Qian Yu, Sumanta Khan, Eli Megidish, Bingran You, Boerge Hemmerling, Andrew Jayich, Juergen Biener, and Hartmut Häffner. 3d-printed micro ion trap technology for scalable quantum information processing, 2023. 8

[44] Sainath Motlakunta, Nikhil Kotibhaskar, Chung-You Shih, Anthony Vogliano, Darian McLaren, Lewis Hahn, Jingwen Zhu, Roland Hablützel, Rajibul Islam, et al. Preserving a qubit during state-destroying operations on an adjacent qubit at a few micrometers distance. *Nature Communications*, 15(1):6575, 2024. Received: 31 July 2023; Accepted: 23 July 2024; Published: 3 August 2024. 8, 12, 13, 16, 17, 28, 47, 48, 65, 66

[45] Austin G. Fowler, Matteo Mariantoni, John M. Martinis, and Andrew N. Cleland. Surface codes: Towards practical large-scale quantum computation. *Phys. Rev. A*, 86:032324, Sep 2012. 9

[46] S. Crain, C. Cahall, G. Vrijsen, E. E. Wollman, M. D. Shaw, V. B. Verma, S. W. Nam, and J. Kim. High-speed low-crosstalk detection of a $^{171}Yb^{+}$ qubit using superconducting nanowire single photon detectors. *Communications Physics*, 2:Article 97, 2019. 11, 17, 29

[47] Lewis Hahn. Developing a robust quantum simulator with trapped ions. Master's thesis, University of Waterloo, 2024. 11

[48] Chung-You Shih. *Holographic Optical Manipulation of Trapped Ions for Quantum Simulation*. PhD thesis, University of Waterloo, 2019. 20, 21, 24, 25, 52

[49] David Blinder, Tobias Birnbaum, Tomoyoshi Ito, and Tomoyoshi Shimobaba. The state-of-the-art in computer generated holography for 3d display. *Light: Advanced Manufacturing*, 3, 06 2022. 23

[50] Dieter Just, Richard Hauck, and Olof Bryngdahl. Rational carrier-period for binarization of sampled images and holograms. *Optics Communications*, 60(6):359–363, 1986. 23

[51] Wai-Hon Lee. Binary computer-generated holograms. *Appl. Opt.*, 18(21):3661–3669, Nov 1979. 23

[52] Philip Zupancic, Philipp M. Preiss, Ruichao Ma, Alexander Lukin, M. Eric Tai, Matthew Rispoli, Rajibul Islam, and Markus Greiner. Ultra-precise holographic beam shaping for microscopic quantum control. *Opt. Express*, 24(13):13881–13893, Jun 2016. 23, 25

[53] Frank Wyrowski. Iterative quantization of digital amplitude holograms. *Appl. Opt.*, 28(18):3864–3870, Sep 1989. 24

[54] Texas Instruments. Dlp9000xuv 0.90 1080p xga ultra-violet dmd. https://www.ti.com/lit/ds/symlink/dlp9000xuv.pdf, 2021. Accessed: July 14, 2025. 33

[55] Chung-You Shih, Jingwen Zhu, and Rajibul Islam. pyslm2: A full-stack python package for holographic beam shaping. *Journal of Open Source Software*, 9(104):6315, 2024. 33

[56] Chung-You Shih. *Programmable Individual Addressing and Floquet Hamiltonian Dynamics in a Trapped Ion Quantum Processor*. PhD thesis, University of Waterloo, 2023. 35

[57] Lukas Postler, Friederike Butt, Ivan Pogorelov, Christian D. Marciniak, Sascha Heußen, Rainer Blatt, Philipp Schindler, Manuel Rispler, Markus Müller, and Thomas Monz. Demonstration of fault-tolerant steane quantum error correction. *PRX Quantum*, 5:030326, Aug 2024. 66